Helsinki University of Technology
Laboratory of Computational Engineering
Espoo 2005 REPORT B51

ANALYSIS AND OPTIMIZATION OF PHOTONIC CRYSTAL COMPONENTS FOR OPTICAL TELECOMMUNICATIONS

Anu Huttunen

Dissertation for the degree of Doctor of Science in Technology to be presented with due permission of the Department of Electrical and Communications Engineering, Helsinki University of Technology, for public examination and debate in Auditorium S1 at Helsinki University of Technology (Espoo, Finland) on the 8th of July, 2005, at 12 noon.

Helsinki University of Technology
Department of Electrical and Communications Engineering
Laboratory of Computational Engineering

Teknillinen korkeakoulu
Sähkö- ja tietoliikennetekniikan osasto
Laskennallisen tekniikan laboratorio

Distribution:
Helsinki University of Technology
Laboratory of Computational Engineering
P. O. Box 9203
FIN-02015 HUT
FINLAND
Tel. +358-9-451 4826
Fax. +358-9-451 4830
http://www.lce.hut.fi

Online in PDF format: http://lib.hut.fi/Diss/2005/isbn9512277611/

E-mail: Anu.Huttunen@hut.fi

ISBN 951-22-7760-3 (printed)
ISBN 951-22-7761-1 (PDF)
ISSN 1455-0474
PicaSet Oy
Espoo 2005

Abstract

Photonic crystals are periodic dielectric structures where the period is of the same order of magnitude than the wavelength of light. As a result of interference, there exist band gaps for light, i.e., light of certain range of frequencies is not allowed to exist inside the photonic crystal, which can be used to control and confine light. In this thesis, photonic crystals were studied with computer simulations and concepts of new components for optical telecommunications were proposed.

An all-optical switch, based on the properties of a Kerr-nonlinear one-dimensional photonic crystal, was investigated. The band gap was shown to change as a function of light intensity inside the nonlinear photonic crystal. Thus, it performs an all-optical switching function, where one signal can be dynamically reflected depending on another signal.

Two parallel waveguides in a two-dimensional photonic crystal were considered. In general, adjacent waveguides are coupled and a light pulse traveling in one waveguide will oscillate between the waveguides. We found complete decoupling between the waveguides for certain geometries. This can be utilized in integrated optics when cross-talk between contiguous channels is not desired.

The band gap of a thin slab of two-dimensional photonic crystal was shown to depend strongly on the material on top/below the slab, and thus a new type of waveguide was proposed. Instead of the conventional defect waveguide, a waveguide can be made by patterning the photonic crystal slab by a suitable material. The waveguiding was shown to be due to band gap difference in some cases and due to average refractive index difference in others.

Microstructure and dual-core fibers were optimized to achieve large negative dispersion and large mode area simultaneously. Negative dispersion fibers are needed for dispersion compensation and pulse compression. They usually have small mode areas and are highly nonlinear, which is a problem for high-intensity applications. This can be avoided with the fiber geometries proposed in this thesis.

The effect of the wavelength dependence of gain, nonlinearity and dispersion to the propagation of short pulses in high-gain efficiency photonic crystal fiber amplifiers was studied. It resulted in asymmetric spectrum and chirp, and reduction of the pulse broadening. Wavelength dependence of the nonlinearity was demonstrated to have the most effect, compared to that of dispersion or gain.

Preface

The work presented in this thesis for the degree of Doctor of Science in Technology has been conducted in the Laboratory of Computational Engineering at Helsinki University of Technology (HUT) during August 2000-May 2005. The work was funded by the Graduate School of Modern Optics and Photonics, the National Graduate School in Materials Physics, the Academy of Finland (Project Nos. 48845, 53903, 205454, 44897 Finnish Center of Excellence Program 2000-2005), and Emil Aaltonen foundation. I would also like to acknowledge the support from the Foundation of Vilho, Yrjö, and Kalle Väisälä.

I am deeply grateful to my supervisor Prof. Päivi Törmä from University of Jyväskylä for her guidance throughout the years. I would also like to acknowledge my collaborators Timo Koponen from University of Jyväskylä, Kari Kataja and Janne Aikio from VTT Electronics, and Karri Varis from HUT Optoelectronics Laboratory for their input to this thesis. I would also like to thank Prof. K. Kaski and Prof. J. Tulkki for the opportunity to work in the Laboratory of Computational Engineering. Finally, I want to thank the coworkers, Mirta Rodriguez, Maria Sammalkorpi, Peter Szelestey, Fredrik Boxberg, Margareta Segerståhl, Eeva Lampinen, Lorna Stimson, Tomasz Rog, and Kaisa Kautto for the excellent working atmosphere and especially Michael Patra for helping me with numerous technical problems.

Anu Huttunen

List of publications

This dissertation consists of an overview and the following publications:

I. A. Huttunen and P. Törmä, *Band structures for nonlinear photonic crystals*, Journal of Applied Physics **91,** 3988–3991 (2002).

II. T. Koponen, A. Huttunen, P. Törmä, *Conditions for waveguide decoupling in square-lattice photonic crystals*, Journal of Applied Physics **96,** 4039–4041 (2004).

III. A. Huttunen, K. Varis, K. Kataja, J. Aikio, and P. Törmä, *Guiding and reflecting light by boundary material*, Optics Communications **244,** 147–152 (2005).

IV. A. Huttunen and P. Törmä, *Optimization of dual-core and microstructure fiber geometries for dispersion compensation and large mode area*, Optics Express **13,** 627–635 (2005).

V. A. Huttunen and P. Törmä, *Effect of wavelength dependence of nonlinearity, gain, and dispersion in photonic crystal fiber amplifiers*, Optics Express **13,** 4286–4295 (2005).

In the overview, these publications are referred to by their roman numerals.

Author's contributions

This dissertation is a review of the author's work in the field of optics, focusing on the properties of photonic crystals. The results are presented in six publications. Anu Huttunen is the principal author of Publications I, III, IV, and V and the second author of Publication II, and she has written all the papers except Publication II.

The author performed all numerical calculations and data analysis in Publications I, III, IV, and V. The author has written the computer programs for Publications I and V. The simulation programs used in the calculations of Publication III were written by the coauthors K. Varis and K. Kataja and by Juuso Olkkonen from VTT Electronics. The calculations in Publication II were performed by T. Koponen. In Publication II, the author contributed to analyzing the results and designing the calculations as well as to writing the paper.

Discussions with Prof. P. Törmä have been extremely helpful throughout the whole work in developing new ideas, designing simulations and analyzing the results.

Additional publication of the author (not included in this thesis):

- A. Huttunen, I. Kallioniemi, and J. Saarinen, *Noninvasive characterization of continuous-profile blazed diffraction gratings*, Applied Optics **40,** 2618–2625 (2001).

Contents

Chapter 1

Introduction

Optical networks have established their existence in telecommunications, as the physical limits of wireless and electronic data transmission capacity have been attained. Yet there is an increasing demand of network capacity due to the growth in the use of internet and real time transmission of voice and picture. The advanced data processing and routing is still performed by electronic switching devices, which are limited in speed. This causes the so-called "electronics bottleneck" and there is a need of all-optical data handling and processing. To perform this task new optical components have to be designed. Photonic crystals are novel optical materials possessing qualities that could not be reached before. They are promising candidates to realize all-optical functions as well as integrated optical circuits or fiber optic components. In this thesis, photonic crystal optical components relevant for optical networks and data processing are designed and studied.

Photonic crystals are periodic structures made of dielectric materials. Regions with different dielectric constants alternate periodically and the period is of the order of the wavelength of light. Then, as light propagates inside the periodic material, it reflects at each interface of the different dielectric materials. As a result of interference, total reflection occurs at specific wavelength-period combinations. Light with this specific wavelength cannot propagate or exist inside the photonic crystal. These forbidden wavelengths or frequencies form a band gap for light, which is the basis of operation of photonic crystals. This phenomenon is also present in the nature: The wings of certain butterflies and moths are covered with periodic microscopic structures, which act as photonic crystals [1]. The wings reflect light that has a wavelength in the band gap of the photonic crystal. This effect is seen as the color of the wings. Also, one-dimensionally periodic structures have been widely used for a long time in various optical components. Well known applications are for example Bragg-mirrors and optical filters.

The concept of photonic crystals was starting to emerge at the end of the 80's, when it was realized that the effect of three-dimensionally periodic media to light

can be thought of being somewhat similar to the effect of semiconductors to electrons [2, 3]. This opened new prospects in photonics. It was realized that the electromagnetic band gap for light would prohibit spontaneous emission [2] or light could be localized when disorder is present in a periodic medium [3]. The experimental search for a photonic band gap structure begun [4]. Meanwhile, the theorists calculated the band structure for light, similar to the electronic band structure in semiconductors, and it was shown that a three-dimensional photonic band gap would exist in a diamond lattice of dielectric spheres [5]. The first three-dimensionally periodic structure exhibiting a photonic band gap in the optical wavelength range was fabricated in the beginning of the 90's [6]. It was called Yablonovite, named after E. Yablonovitch, the inventor of the structure. It was fabricated by drilling three sets of holes in specified angles into a solid slab of semiconductor and had a band gap in the microwave region. Implanting defects into Yablonovite [7] and the possibility of a single-mode light-emitting diode (LED) using a photonic crystal cavity were envisioned [8].

Since the realization of a three-dimensionally periodic structure with micrometer size features was very difficult, there were experiments [9, 10] and theory [11, 12] done with two-dimensionally periodic structures exhibiting band gaps. A true photonic crystal is periodic in all three directions and thus can have such a band gap that light is not allowed to propagate in any direction. However, structures that are periodic in only one or two dimensions are also called one- and two-dimensional photonic crystals, respectively. Although they are not photonic crystals in the strict sense, they posses similar properties, if only in the direction of the periodicity. Line defects in two-dimensional photonic crystals were predicted to act as waveguides, and point defects as microcavities [13]. In these new photonic crystal waveguides light would follow a sharp 90º bend with almost 100% transmission over a broad frequency range [14].

It was not until the end of the 90's when a structure with a photonic band gap in the infrared frequencies was first realized with a face-centered-cubic lattice of metallic squares [15]. It was not very applicable at optical wavelengths, however, due to strong attenuation. Band gap in the infrared frequencies with a dielectric structure was first realized with the woodpile structure that consists of tiny rods of silicon piled up in a layer by layer manner [16]. The same geometry was also used to construct the first photonic crystal for the wavelengths used in the telecommunications, 1.3 and 1.5 μm [17]. In order to incorporate active photonic devices, the woodpile structure was also fabricated from GaAs and InP instead of silicon [18].

Nowadays, three- and two-dimensional photonic crystals can be fabricated with established fabrication methods and various components have been realized, see Refs. [19–22] and references therein. Two-dimensional photonic crystals and photonic crystal slabs, which have a finite thickness in the vertical direction, have been used to fabricate for example waveguides [23, 24], microcavities [25–27],

add-drop devices [28], and lasers [29–31]. Three-dimensional photonic crystals have been used for microcavities, light-emitting diodes (LEDs) and lasers [32]. Nonlinear photonic crystals have been demonstrated to exhibit all-optical switching behavior and optical bistability [33].

Photonic crystal fibers, for their part, have revolutionized fiber optics. Many of the limits of fiber optics have been overcome with this new class of fibers. A photonic crystal fiber has a periodic cross section, i.e., the cladding of the fiber is periodic in the plane that is perpendicular to the direction of propagation of light in the fiber. When the cladding lattice constitutes a photonic crystal, light can be confined to the core by the band gap effect [34]. Thus in a photonic crystal fiber, the core can have a lower refractive index than the cladding, and light can be guided for example in air [35]. Even if light is not confined to the core by the band gap, but only by the average refractive index difference, photonic crystal fibers exhibit special characteristics that cannot be achieved with standard optical fibers. These characteristics are single mode operation for all wavelengths [36–38], freedom for the design of their dispersion properties [39–42], and the possibility to fabricate fibers with extremely large or small mode areas [43, 44]. Photonic crystal fibers have been used for example in nonlinear optics and in fiber lasers, see Refs. [45–47] and references therein.

Chapter 2

Photonic crystals

Photonic crystals are periodic structures where the length of the period is of the order of the wavelength of light. Due to the wave nature of light and interference caused by the periodic structure, there exists a band gap for light in photonic crystals. In order to accurately describe the behavior of light in photonic crystals, the full vector nature of light has to be taken into account using the Maxwell's equations.

2.1 Maxwell's equations

The macroscopic electromagnetic fields, the electric field $\mathbf{E}(\mathbf{r}, t)$, the magnetic field $\mathbf{H}(\mathbf{r}, t)$, the electric flux density $\mathbf{D}(\mathbf{r}, t)$, and the magnetic flux density $\mathbf{B}(\mathbf{r}, t)$, are described by the Maxwell's equations

$$\nabla \cdot \mathbf{B}(\mathbf{r}, t) = 0 \tag{2.1}$$

$$\nabla \cdot \mathbf{D}(\mathbf{r}, t) = 4\pi\rho(\mathbf{r}, t) \tag{2.2}$$

$$\nabla \times \mathbf{E}(\mathbf{r}, t) + \frac{1}{c}\frac{\partial \mathbf{B}(\mathbf{r}, t)}{\partial t} = 0 \tag{2.3}$$

$$\nabla \times \mathbf{H}(\mathbf{r}, t) - \frac{1}{c}\frac{\partial \mathbf{D}(\mathbf{r}, t)}{\partial t} = \frac{4\pi}{c}\mathbf{J}(\mathbf{r}, t), \tag{2.4}$$

where $\rho(\mathbf{r}, t)$ and $\mathbf{J}(\mathbf{r}, t)$ are the free electric charge and current densities, respectively, and c is the speed of light. Here, the Maxwell's equations are presented in cgs units, since these units are customarily used in the calculation of band structures of photonic crystals [13]. The same units are also used in Section 4.1.1 where the Fourier-method for the calculation of the band structures of nonlinear photonic crystals is introduced. However, SI units are used in context with the pseudo-spectral method in Section 4.1.2, the finite difference time domain method in Section 4.2.1, and the optical nonlinear Schrödinger equation in Appendix B.

To simplify the Maxwell's equations, a few assumptions can be made. The electric and magnetic fields can be assumed to be time-harmonic

$$\mathbf{H}(\mathbf{r}, t) = \mathbf{H}(\mathbf{r})e^{i\omega t} \tag{2.5}$$

$$\mathbf{E}(\mathbf{r}, t) = \mathbf{E}(\mathbf{r})e^{i\omega t}, \tag{2.6}$$

where ω is the angular frequency of the electromagnetic wave. The actual fields are the real parts of the complex valued fields in Eqs. (2.5) and (2.6). Furthermore, for a linear, macroscopic, and isotropic material, the constitutive equations relating the fields to the flux densities are

$$\mathbf{D}(\mathbf{r}) = \varepsilon(\mathbf{r})\mathbf{E}(\mathbf{r}) \tag{2.7}$$

$$\mathbf{B}(\mathbf{r}) = \mu(\mathbf{r})\mathbf{H}(\mathbf{r}), \tag{2.8}$$

where $\varepsilon(\mathbf{r})$ is the dielectric constant and $\mu(\mathbf{r})$ is the magnetic permeability of the material. Nonmagnetic medium is assumed and thus $\mu(\mathbf{r}) = \mu_0$, where μ_0 is the magnetic permeability of vacuum. Also, the considered materials are assumed to have no free charges or currents: $\rho = \mathbf{J} = 0$. Thus, the Maxwell's equations are reduced to

$$\nabla \cdot \mathbf{H}(\mathbf{r}) = 0 \tag{2.9}$$

$$\nabla \cdot [\varepsilon(\mathbf{r})\mathbf{E}(\mathbf{r})] = 0 \tag{2.10}$$

$$\nabla \times \mathbf{E}(\mathbf{r}) + \frac{i\omega}{c}\mathbf{H}(\mathbf{r}) = 0 \tag{2.11}$$

$$\nabla \times \mathbf{H}(\mathbf{r}, t) - \frac{i\omega}{c}\varepsilon(\mathbf{r})\mathbf{E}(\mathbf{r}) = 0. \tag{2.12}$$

The properties of the photonic crystals can be deduced from these equations.

2.2 Electromagnetic modes

Following the approach of Ref. [13], Eqs. (2.11) and (2.12) are combined into one equation called the master equation

$$\nabla \times \left[\frac{1}{\varepsilon(\mathbf{r})}\nabla \times \mathbf{H}(\mathbf{r})\right] = \left(\frac{\omega}{c}\right)^2 \mathbf{H}(\mathbf{r}). \tag{2.13}$$

The solution of this equation completely determines the fields [the divergence in Eq. (2.9) has to be valid simultaneously]. The electric field can be deduced from

$$\mathbf{E}(\mathbf{r}) = \left[\frac{-ic}{\omega\varepsilon(\mathbf{r})}\right]\nabla \times \mathbf{H}(\mathbf{r}). \tag{2.14}$$

Equation (2.13) is an eigenvalue equation of the form

$$\mathbf{A}\mathbf{H}(\mathbf{r}) = \left(\frac{\omega}{c}\right)^2 \mathbf{H}(\mathbf{r}), \tag{2.15}$$

where **A** is an operator acting on an eigenfunction **H(r)** with an eigenvalue $(\omega/c)^2$. The eigenfunctions **H(r)** are the allowed fields in the structure, i.e., the electromagnetic modes of the system. The operator **A** is linear and thus any linear combination of the solutions is also a solution. The operator **A** is also Hermitian and thus any two modes with different energies are orthogonal.

An important feature of the electromagnetic modes is that there is no specified length scale involved. Once the eigenvalues and eigenfunctions of Eq. (2.13) are solved, they can be scaled to any physical size or wavelength range. This can be understood by defining $\mathbf{r}' = s\mathbf{r}$, $\nabla' = \nabla/s$, and $\varepsilon'(\mathbf{r}) = \varepsilon(\mathbf{r}/s)$ and substituting them into Eq. (2.13). This results in

$$s\nabla' \times \left[\frac{1}{\varepsilon(\mathbf{r}'/s)} s\nabla' \times \mathbf{H}(\mathbf{r}'/s)\right] = \left(\frac{\omega}{c}\right)^2 \mathbf{H}(\mathbf{r}'/s), \tag{2.16}$$

where $\varepsilon(\mathbf{r}'/s) = \varepsilon'(\mathbf{r}')$. Thus

$$\nabla' \times \left[\frac{1}{\varepsilon'(\mathbf{r}')} \nabla' \times \mathbf{H}(\mathbf{r}'/s)\right] = \left(\frac{\omega}{cs}\right)^2 \mathbf{H}(\mathbf{r}'/s). \tag{2.17}$$

It can be seen that when the dimensions are scaled by a factor of s, the electromagnetic mode is the same, but has to be scaled as $\mathbf{H}(\mathbf{r}'/s)$ and the frequency has to be scaled as ω/s. Due to the scalability, photonic crystal components can be designed without specifying the dimensions and subsequently fabricated in any scale to perform experiments in varying wavelength ranges.

2.3 Photonic band structures

The photonic band structure is the relation between the wave vector **k** and the frequency ω of light. In a homogeneous material the relation is a line whose slope is proportional to the refractive index. In a periodic material, however, the frequency as a function of the wave vector forms bands which can be separated by band gaps. The photonic band structures stem from symmetry considerations.

In a system with continuous translational symmetry (homogeneous material) the dielectric constant is invariant with respect to any translation described by a translation operator $\mathbf{T}_d$. Since the system does not change with respect to position, one has $\mathbf{T}_d\varepsilon(\mathbf{r}) = \varepsilon(\mathbf{r}+\mathbf{d}) = \varepsilon(\mathbf{r})$ for any vector **d**. If the eigenmode of the system **H(r)** [see Eq. (2.15)] is translated by a vector **d** and then translated back by $-\mathbf{d}$, it has to be unchanged. Thus $\mathbf{T}_d^{-1}\mathbf{A}\mathbf{T}_d$=**A**, which means that the operators **A** and $\mathbf{T}_d$ commute. This in turn indicates that $\mathbf{T}_d\mathbf{H}$ is also an eigenmode of **A** with the

same frequency as **H**. If there is no degeneracy in the system, $\mathbf{T}_d\mathbf{H}$ can differ from **H** only by multiplication with a constant. This suggests that the eigenmodes are of the form $\exp[i(\mathbf{k}\cdot\mathbf{r})]$, since

$$\mathbf{T}_d e^{i(\mathbf{k}\cdot\mathbf{r})} = e^{i(\mathbf{k}\cdot(\mathbf{r}+\mathbf{d}))} = e^{i(\mathbf{k}\cdot\mathbf{d})}e^{i(\mathbf{k}\cdot\mathbf{r})}, \tag{2.18}$$

where $\exp[i(\mathbf{k}\cdot\mathbf{d})]$ is a constant. For example, in free space the electromagnetic modes are of the form of plane waves $\mathbf{H}_\mathbf{k}(\mathbf{r}) = \mathbf{H}_0\exp[i(\mathbf{k}\cdot\mathbf{r})]$, where $\mathbf{H}_0$ is a constant vector.

Photonic crystals are periodic and thus have discrete translational symmetry. The system is invariant under a translation with a vector

$$\mathbf{R} = jP_x\mathbf{x} + lP_y\mathbf{y} + mP_z\mathbf{z} \tag{2.19}$$

that is an integer multiple (j, l, and m are integers) of the period of the photonic crystal $P_{x,y,z}$ in each direction

$$\mathbf{T}_\mathbf{R} e^{i(\mathbf{k}\cdot\mathbf{r})} = e^{i(\mathbf{k}\cdot(\mathbf{r}+\mathbf{R}))} = e^{i(\mathbf{k}\cdot\mathbf{R})}e^{i(\mathbf{k}\cdot\mathbf{r})}. \tag{2.20}$$

The primitive reciprocal lattice vector is defined as

$$\mathbf{G} = (2\pi p/P_x)\mathbf{x} + (2\pi q/P_y)\mathbf{y} + (2\pi s/P_z)\mathbf{z}, \tag{2.21}$$

where p, q, and s are integers. It can be seen that the eigenvalue of Eq. (2.20) for wavevectors **k** and $\mathbf{k}+\mathbf{G}$ is the same: $\exp[i(\mathbf{k}\cdot\mathbf{R})] = \exp[i((\mathbf{k}+\mathbf{G})\cdot\mathbf{R})] = \exp[i(k_x jP_x + k_y lP_y + k_z mP_z)]$. Then the eigenfunctions are degenerate and any superposition of the degenerate eigenfunctions is also an eigenfunction for a wavevector **k** (or **k**+**G**)

$$\mathbf{H}_\mathbf{k}(\mathbf{r}) = \sum_\mathbf{G} C_\mathbf{G} e^{i[(\mathbf{k}+\mathbf{G})\cdot\mathbf{r}]} = e^{i(\mathbf{k}\cdot\mathbf{r})}\sum_\mathbf{G} C_\mathbf{G} e^{i(\mathbf{G}\cdot\mathbf{r})}, \tag{2.22}$$

where the $C_\mathbf{G}$ are constants. This type of function satisfies the Bloch's theorem

$$\mathbf{H}_\mathbf{k}(\mathbf{r}) = e^{i(\mathbf{k}\cdot\mathbf{r})}\mathbf{u}_\mathbf{k}(\mathbf{r}) \tag{2.23}$$

where

$$\mathbf{u}_\mathbf{k}(\mathbf{r}) = \mathbf{u}_\mathbf{k}(\mathbf{r}+\mathbf{R}). \tag{2.24}$$

This means that any eigenfunction can be written as a product of a plane wave and a periodic function. When Eq. (2.23) is substituted to Eq. (2.13), one gets

$$(i\mathbf{k}+\nabla)\times\left[\frac{1}{\varepsilon(\mathbf{r})}(i\mathbf{k}+\nabla)\times\mathbf{u}_\mathbf{k}(\mathbf{r})\right] = \left[\frac{\omega(\mathbf{k})}{c}\right]^2\mathbf{u}_\mathbf{k}(\mathbf{r}). \tag{2.25}$$

Here, **k** enters the equation as a parameter. Equation (2.25) is an eigenvalue equation for which $\mathbf{u}_\mathbf{k}(\mathbf{r})$ is the eigenfunction and $(\omega(\mathbf{k})/c)^2$ is the eigenvalue. When

the periodic boundary condition (2.24) is imposed, the eigenvalues get discretized $(\omega_n(\mathbf{k})/c)^2$, where n denotes the index of the discrete eigenvalues. When the eigenvalue equation (2.25) is solved, one gets n solutions $\mathbf{u}_{\mathbf{k},n}(\mathbf{r})$ and n eigenvalues $(\omega_n(\mathbf{k})/c)^2$. Thus for every predetermined value of $\mathbf{k}$, there are n solutions with frequencies $\omega_n(\mathbf{k})$. The relations $\omega_n(\mathbf{k})$ as a function on $\mathbf{k}$, each with an index n, constitute the photonic bands, i.e., the photonic band structure. A band gap consists of a range of frequencies for which there is no solution for any wavevector $\mathbf{k}$.

It can be seen from Eq. (2.22) that Bloch states $\mathbf{u}_{\mathbf{k}}(\mathbf{r})$ and $\mathbf{u}_{\mathbf{k}+\mathbf{G}}(\mathbf{r})$ are equal, as are the states for any sum of the wavevector and integer multiples of the reciprocal lattice vector. Thus it is adequate to consider wavevector values is the range

$$-\pi/P_\nu < k_\nu \leq \pi/P_\nu, \text{ where } \nu = x, y, z \tag{2.26}$$

when solving the eigenvalue equation Eq. (2.25). Equation (2.26) defines the Brilliouin zone.

2.4 Photonic crystal components

In order to construct a photonic crystal component, one first has to find a photonic crystal geometry that has a band gap, i.e., range of frequencies for which there are no allowed electromagnetic modes. Then it is possible to make a defect in the lattice that permits one or more localized modes that have frequencies in the band gap. In this way for example waveguides and microcavities can be formed. A waveguide is a linear defect along which light with a wavelength corresponding to the defect mode frequency can propagate. A microcavity is a point defect that can support a localized mode.

Photonic crystals that are periodic in all three dimensions are called three-dimensional (3D) photonic crystals and they are the only true photonic crystals in the strict sense since in them light propagation can be forbidden in all directions. The first 3D photonic crystal was the Yablonovite [6], the symmetry of which resembles the diamond lattice. It was fabricated by drilling holes to three directions into a slab of dielectric at an angle 35.26º away from the normal and 120º from each others at the azimuth [see Fig. 2.1 (a)]. Later on, the woodpile structure [16] which has a face-centered-tetragonal lattice [see Fig. 2.1 (b)], and the inverse-opal structure [48] which is a face centered cubic lattice of air spheres in a silicon backbone, were verified to exhibit band gaps.

Structures that are periodic in two dimensions are called two-dimensional (2D) photonic crystals and they can have a band gap for in-plane propagation of light. Two-dimensional photonic crystals can consist of, for example, dielectric rods in air or air holes in a dielectric organized in a square- or hexagonal lattice (see Fig.2.2). Most 2D photonic crystals have a band gap for sufficiently high

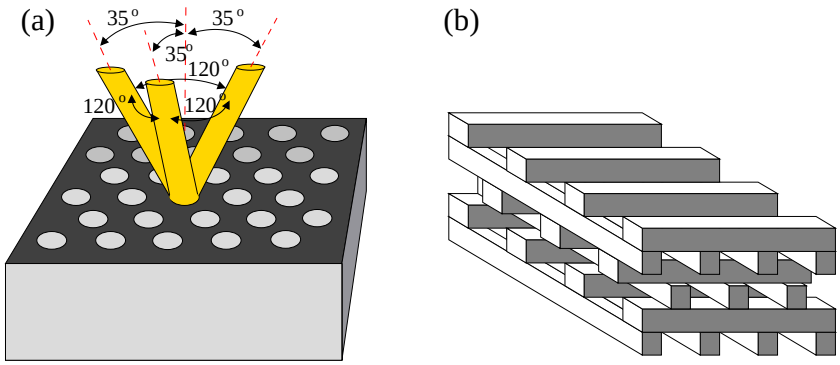

Figure 2.1: (a) Yablonovite is fabricated by covering a slab with a mask that has holes arranged in a hexagonal lattice and drilling through each hole in three specific directions. (b) Woodpile structure is composed of tiny rods that are arranged periodically. The rods are stacked so that the sequence is repeated after every four layers.

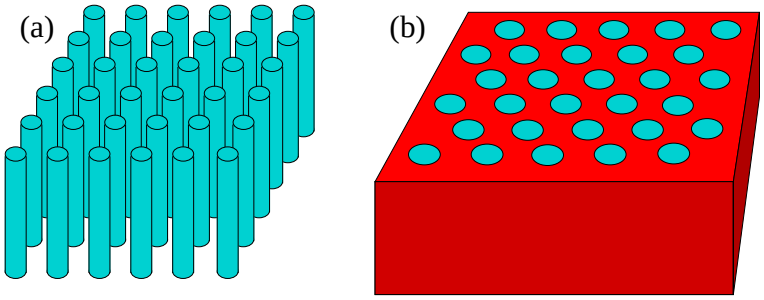

Figure 2.2: (a) Dielectric rods in air arranged in a square lattice. (b) Air holes in dielectric arranged in a hexagonal lattice.

dielectric contrast, i.e., difference between the dielectric constants of the materials. Many 2D photonic crystal devices are constructed of photonic crystal slabs, which have a finite thickness (usually less than one period of the photonic crystal) in the direction perpendicular to the periodic lattice. Thus light is confined by the band gap in the plane of the 2D photonic crystal and by total internal reflection in the vertical direction. A waveguide-coupled photonic crystal slab has been shown to exhibit a strong 2D bandgap at the wavelength often used in telecommunications 1.5 μm [49].

Structures that are periodic in one direction only are called one-dimensional photonic crystals. These structures (Bragg reflectors) have been used for a long time before the concept of photonic crystals was established, but the same concepts and principle apply to the one-dimensional structures also. One-dimensional photonic crystals have been used for example in a refractometer to detect refract-

ive indices of materials [50].

Since a photonic crystal waveguide operates based on the band gap effect, rather than the refractive index difference as the conventional waveguides, sharp turns can be realized with them. The first experimental demonstration of guiding and bending of electromagnetic waves in a photonic crystal waveguide showed near 100% transmission around a 90º bend for millimeter waves [23]. A waveguide for the telecommunications wavelength range of 1.47-1.6μm was demonstrated later [24]. A comparative study between photonic crystal defect waveguides and ridge waveguides showed less propagation losses for the photonic crystal waveguides [51].

Microcavities are used in light-emitting diode structures and laser systems as resonant cavities. They can be characterized by a quality factor Q, which is defined as [52]

$$Q = \frac{2\pi \cdot \text{stored energy}}{\text{energy loss per cycle}}. \tag{2.27}$$

As the microcavity traps light in a specified frequency range, they can be used to reduce the linewidth of a light-emitting diode. The microcavities can also reduce the lasing threshold of semiconductor lasers by changing the available density of states for electromagnetic modes. The light output of a light emitting diode can also increase as the spontaneous emission rate is enhanced by coupling an optical transition to the microcavity resonance. The first microcavity in a three-dimensional photonic crystal in the microwave regime was demonstrated by planting a defect in the Yablonovite [7]. One of the first microcavities in a two-dimensional photonic crystal demonstrated a cavity Q value of 23000 in the millimeter wavelength range [53]. The photonic crystal consisted of a square lattice of 10 cm long cylindrical alumina-ceramic rods. In another experiment a one-dimensional photonic crystal (holes) was integrated directly into a submicrometer-scale silicon waveguide [25]. It exhibited microcavity resonances with a Q value of 265 for wavelength 1.56 μm and an extremely small modal volume. In a 2D photonic crystal slab (air holes in a dielectric), a high Q nanocavity with Q=45000 and a small modal volume V resulted in a Q/V ratio 10-100 times larger than in previous studies [26]. Recently, nanocavities with an extremely high Q factor of 600 000 have been realized in a 2D photonic crystal slab for the wavelength 1.57 μm. The cavity was formed by a double-heterostructure consisting of a waveguide and photonic crystals (air holes in dielectric) with two different periods [27]. Quality factors exceeding 20 000 000 have been predicted to be obtainable using this technique.

By incorporating active materials, photonic crystal microcavities can be used as laser cavities. A two-dimensional photonic band-gap defect mode laser was shown to exhibit peak emission at 1.55 μm [29]. The photonic crystal consisted of a hexagonal array of air holes in a thin semiconductor membrane. The membrane was half a wavelength thick, confining light vertically by total internal re-

flection. The cavity was formed by a single missing air hole and the light was emitted vertically. A quantum cascade tunable laser was demonstrated using a 2D photonic crystal to simultaneously provide feedback for the laser action and diffract light vertically [31]. The photonic crystal did not have a complete band gap, but strongly dispersive flat-bands were used. Control of light emission at 1.55 μm in a three-dimensional photonic crystal (woodpile structure with point defects) has also been demonstrated [32]. Light emission was well suppressed in regions of complete photonic band gap and strong emission was observed at the defect states. The defect-mode emission is enhanced since other leakage paths are suppressed. In another experiment the spontaneous emission from a semiconductor quantum dot was controlled using the host photonic crystal. The spectral distribution of the inhibited and enhanced decay rates were seen to depend on the photonic crystal parameters [54]. Photonic crystals can be used to modify the spontaneous emission rate even when there are no defects in the structure, for example, when light emitters are incorporated in an inverse opal structure [55].

An add-drop device has been demonstrated by combining a waveguide and microcavities in a 2D photonic crystal [56]. It consists of a waveguide and isolated defects close to it. As light propagates in the waveguide, photons are trapped by the cavity resonances and emitted to free space [56]. Drop function for seven wavelengths around 1.5 μm was realized by combining regions of photonic crystals with seven different lattice constants [57]. Each photonic crystal region has a line-defect waveguide with a row of missing air holes and a point-defect cavity with three missing holes. The different regions are scaled in size to drop a certain wavelength.

Photonic crystals can also have dynamic properties. Inverse opal structure infiltrated by a low refractive index liquid crystal with strong anisotropy was theoretically shown to exhibit the opening and closing of the band gap by changing the orientation of the nematic director [58]. This allows for tunability of spontaneous emission, waveguiding effects, and light localization. A tunable photonic crystal using liquid crystals has been realized for example in Ref. [59].

In all-optical signal processing one needs to control light with light. Thus nonlinear materials that change their properties when light is present are needed. Usually, however, the nonlinear effects are very weak, but with photonic crystal devices the nonlinear interaction can be enhanced [33]. All-optical switching using one-dimensional nonlinear photonic crystals has been widely investigated both numerically and theoretically [60–65]. The basis of the operation of these devices is that once the refractive index of the nonlinear material is changed with a light field, the band gap of the photonic crystal changes and thus the reflectance of another light field can be all-optically influenced. All-optical switching in one-dimensionally periodic structures has also been experimentally explored [66–69]. Similarly, in a two-dimensional photonic crystal the band edge can be tuned, which has been experimentally demonstrated [70–73]. A Mach-Zehnder type all-

optical switch has also been fabricated using a 2D photonic crystal [74]. Optical switching in a 3D photonic crystal has also been experimentally verified [75].

Nonlinear photonic crystal structures can exhibit bistable behavior, which can lead to the development of all-optical transistors and logical gates or optical memory [33]. A bistable device exhibits a hysteresis relation between input and output signals. Bistable behavior has been demonstrated in a 1D photonic crystal [76, 77]. In 2D photonic crystals, bistable switching has been studied in a resonant tunneling device, which consists of a cavity which is coupled to waveguides and one can switch the defect mode frequency [78–80]. This has been also experimentally demonstrated [81].

2.5 Fabrication methods

The most popular 3D photonic crystal has been the woodpile structure [16, 17, 82]. Woodpile photonic crystals are fabricated by repetitive deposition and etching of multiple dielectric films of silicon using well developed and supported Si integrated circuit fabrication processes. Woodpile structures consisting of III-V semiconductors have been fabricated by stacking stripe-patterned wafers with a precise alignment technique and wafer-fusing them [18, 28, 83]. Since the woodpile structures are fabricated with lithographic procedures, their thickness in the growth direction is only a couple of unit cells. Larger woodpile structures have been produced by preparing unit plates using a single sequence of an integrated circuit process and then accurately aligning the lattices by micromanipulation [84]. Since the woodpile structures are fabricated layer by layer, defects can be accurately positioned inside them.

Considerably larger three-dimensionally periodic structures can be fabricated by spontaneous crystallization of colloids, i.e., hard particles in suspension. The polymer or silica microspheres naturally self-assemble from colloidal suspension into a solid, three-dimensionally periodic structure, which can then act as a template for construction of the photonic crystal. Photonic crystals exhibiting complete band gaps near 1.5 μm [48] and 1.3 μm [85] were fabricated by synthesis of silicon inverse-opal structure. Lattice of mono-disperse silica spheres was used as a template for silicon infiltration. Silicon was grown inside the voids of the opal template by means of chemical vapour deposition and the silica template was subsequently removed. The drawback of the inverse-opal structures is that the band gap is small due to the face-centered-cubic and hexagonal-close-packed geometries. Also the purity of the structures has been poor.

Another method to fabricate large-scale 3D photonic crystal structures with sub-micrometer periodicity is the 3D holographic lithography, see Refs. [86, 87] and references therein. In holographic lithography, a film of photoresist is illuminated by the interference pattern of four non-coplanar laser beams and the

unexposed areas are subsequently dissolved. This results in polymeric structures, which are used as templates to create complementary dielectric structures with high refractive-index contrast. However, the inclusion of defects in the periodic structures constructed by holographic or self-assembly methods is difficult.

Large photonic crystals of square spiral posts in a tetragonal lattice have also been proposed to be conceivable by large scale microfabrication using glancing angle deposition techniques [88]. The technique combines oblique vapour deposition and precisely controlled motion of a two-dimensionally patterned substrate.

There are also other layer-by-layer structures than the woodpile structure exhibiting 3D photonic band gaps that can be fabricated by lithographic methods. One consists of an alternating stack of 2D photonic crystal structures: dielectric rods in air and air holes in dielectric where designed point defects can be flexibly introduced [89, 90]. Another proposed geometry consists of alternating layers of rods and veins [91].

The first 2D photonic crystals were fabricated by microassembly, which was feasible due to the large enough size of the dielectric cylinders [9] and the alumina-ceramic rods [10] in question. These photonic crystals operated in the centi- and millimeter wavelength range. However, more sophisticated fabrication methods are needed when the structures are scaled down. Macroporous silicon was demonstrated to have a band gap centered at 5 μm [92]. It was fabricated by electrochemical etching in hydrofluoric acid and resulted in uniform pores with a diameter in the micrometer range and a depth of several hundreds of micrometers. Two-dimensional band gap in the visible wavelength range was shown in nanochannel glasses which are a regular array of air cylinders fabricated by a fiber draw process [93]. The most popular way to fabricate 2D photonic crystals is, however, electron beam lithography and etching of semiconductor materials. A 2D photonic crystal for 1.47-1.6μm has been fabricated by electron beam lithography and dry etching on a GaInAsP thin film [24]. A 2D photonic crystal slab has been fabricated by first growing a semiconductor (InGaAsP) layer by metal-organic vapour phase epitaxy. Then a resist mask, with the photonic crystal pattern, was coated on the semiconductor layer by electron beam lithography and the resist pattern was transferred to the semiconductor layer by reactive ion etching [28].

Chapter 3

Photonic crystal fibers

Photonic crystal fibers have a cladding that is periodic in the plane of the cross-section of the fiber, i.e., perpendicular to the propagation direction. In most cases the periodic pattern consists of air holes in a dielectric (often silica), but other configurations have also been explored. The periodic cladding can confine light to the core with two different mechanisms. If the frequency of the light is in the band gap of the two-dimensional photonic crystal formed by the periodic cladding, light is guided by the photonic band gap effect. In this case light can be guided even in air core, i.e., the index of the core can be lower than that of the cladding. If the light frequency is not in the band gap of the periodic cladding structure, light is guided by refractive index difference as in conventional optical fibers. In this case the fiber is called microstructure fiber. The modal and dispersion properties of photonic crystal/microstructure fibers are very different from standard optical fiber.

3.1 Light propagation in optical fiber

Light propagation in photonic crystal or microstructure fibers can be described similarly to step index fiber by the optical nonlinear Schrödinger equation [94] (the details are shown in Appendix B)

$$\begin{aligned}\frac{\partial A}{\partial z} = &-\sum_{n=2}^{M}\frac{i^{n+1}}{n!}\beta_n\frac{\partial^n A}{\partial T^n} - \frac{\alpha A}{2}\\ &+ i\gamma\left(1+\frac{i}{\omega_0}\frac{\partial}{\partial T}\right)A(z,t)\int_{-\infty}^{\infty}R(T')|A(z,T-T')|^2dT'.\end{aligned} \tag{3.1}$$

The electric field is assumed to be of the form

$$\mathbf{E}(\mathbf{r},t) = \mathbf{x}\frac{1}{2}\{F(x,y)A(z,t)e^{i\beta_0 z-\omega_0 t}+c.c.\}, \tag{3.2}$$

where $A(z,t)$ is the slowly varying envelope of the pulse, $F(x,y)$ represents the transversal eigenmode distribution of the fiber, β_0 is the propagation constant of the eigenmode and ω_0 is the center frequency of the pulse. Here, Eq. (3.1) is represented in a reference frame moving at the group velocity, i.e., $T = t - \beta_1 z$. The first term on the right side of Eq. (3.1) describes dispersion, and the second and third terms describe attenuation and nonlinear effects, respectively. The β_n are the dispersion coefficients, α is the attenuation constant, γ is the nonlinearity coefficient, and R is the nonlinear response function.

The refractive index that light experiences in optical fiber depends on the light frequency. This phenomenon is called chromatic dispersion and it broadens optical pulses as the different frequency components of the pulse travel with different speeds. Dispersion consists of two parts: material dispersion and waveguide dispersion. Material dispersion originates from the frequency dependence of the refractive index of silica (or other dielectric). Waveguide dispersion originates from the frequency dependence of a specific mode of the fiber: the mode distributions of the fiber change with the wavelength and thus they experience different effective indices as a function of the wavelength. Dispersion effects are included in the optical nonlinear Schrödinger equation (3.1) through the β_n terms which are the derivatives of the propagation constant with respect to the frequency, forming a Taylor series representation of the propagation constant with respect to the frequency. The group velocity dispersion parameter is the second derivative of the propagation constant $\beta_2 = d^2\beta/d\omega^2$. When $\beta_2 > 0$, the dispersion is called normal dispersion and when $\beta_2 < 0$, anomalous dispersion. The magnitude of the dispersion is often characterized by the dispersion parameter

$$D = -\frac{\lambda}{c}\frac{d^2 n}{d\lambda^2} = -\frac{2\pi c}{\lambda^2}\beta_2. \tag{3.3}$$

The dispersion length is the distance during which the dispersive effects become important and it is defined as

$$L_D = \frac{T_0^2}{|\beta_2|}, \tag{3.4}$$

where T_0 is the pulse length.

When the intensity of light is high enough (as is often the case for optical fibers since light is confined to a small area), nonlinear effects change the pulse spectrum while light is propagating in the fiber. The mechanisms that are responsible for this are for example third-order harmonic generation, four-wave mixing, and nonlinear refraction which results from the intensity dependence of the refractive index. Nonlinear refraction leads to self-phase modulation: the pulse changes its own phase since the refractive index is dependent on the intensity of the pulse itself. Cross-phase modulation means that pulses affect each others' phases by inducing intensity dependent changes in the refractive index. The nonlinear effects also

include the stimulated Raman scattering which results from inelastic scattering of photons in the material. Part of the photon energy is absorbed by a vibrational excitation and thus the photon frequency is downshifted. The nonlinear effects are described by the last term in Eq. (3.1). The nonlinearity coefficient is

$$\gamma = \frac{n_2 \omega_0}{c A_{eff}}, \tag{3.5}$$

where n_2 is the nonlinear-index coefficient and the effective mode area is

$$A_{eff} = \frac{\left(\int_{-\infty}^{\infty}\int_{-\infty}^{\infty} |F(x,y)|^2 dxdy\right)^2}{\int_{-\infty}^{\infty}\int_{-\infty}^{\infty} |F(x,y)|^4 dxdy}. \tag{3.6}$$

The distance after which the nonlinear effects are important is called the nonlinear length

$$L_{NL} = \frac{1}{\gamma P_0}, \tag{3.7}$$

where P_0 is the peak power of the pulse.

There can exist a special solution to Eq. (3.1) in the anomalous dispersion regime, when dispersion and nonlinear effects cancel each other. The solution is called a soliton. The form of the fundamental soliton can be solved analytically and it is

$$U(\xi, \tau) = e^{i\xi/2} \mathrm{sech}\tau, \tag{3.8}$$

where $\tau = T/T_0$ and $\xi = z/L_D$. One can see that the shape of the soliton does not depend on the z-coordinate which means that a soliton propagates along a fiber with no change in the shape. Thus the solitons can propagate through extremely long lengths of fiber without broadening. There also exists higher-order solitons that undergo periodic changes in their shape while propagating in the fiber. Because of their remarkable properties, the solitons have many potential applications, for example, in time division multiplexed networks.

3.2 Modal properties

One of the most important properties of the photonic crystal and microstructure fibers that make them superior to standard optical fiber is that they can be designed to be endlessly single-mode. It means that such a photonic crystal fiber is single mode for all wavelengths. This is not achievable with a step index fiber. The number of guided modes in a step index fiber is determined by the normalized frequency V_{SIF} which is defined as [94]

$$V_{SIF} = \frac{2\pi R_{core}}{\lambda} \sqrt{n_{core}^2 - n_{clad}^2}, \tag{3.9}$$

where R_{core} is the core radius, and n_{core} and n_{clad} are the core and cladding refractive indices, respectively. The fiber modes are determined from the eigenequation (B.17) and each mode has a propagation constant β. When the propagation constants of the modes are plotted as a function of the normalized frequency V_{SIF}, it can be seen that there exists only one mode for $V_{SIF} < 2.405$ [95]. The single mode operation is assured by choosing a proper core radius and refractive indices for the wavelength range in question. However, the fiber becomes multimode for sufficiently small wavelengths in any case as can be seen from Eq. (3.9).

The single mode condition for photonic crystal fiber is very different as was already noticed in the first experiments [36, 37]. The reason is the microstructure geometry of the fiber. At short wavelengths, light can penetrate the high index regions of the cladding (i.e., avoid the air holes), which increases the effective cladding index. Thus the refractive index difference $n_{core}^2 - n_{clad}^2$ decreases, when $\lambda \to 0$, and the V parameter can stay bounded for all wavelengths. The normalized frequency for a photonic crystal fiber has to be defined differently from step index fiber since there is no well-defined core radius [38]

$$V_{PCF} = \frac{2\pi P}{\lambda}\sqrt{n_{core}(\lambda)^2 - n_{clad}(\lambda)^2}, \tag{3.10}$$

where P is the period of the cladding lattice and the wavelength dependence of the core and cladding refractive indices has been included. Here the core refractive index is defined as the effective index $n_{core}(\lambda) = c\beta/\omega$, where β is the propagation constant of the mode and $n_{clad}(\lambda)$ is the effective index of the cladding lattice (without the core). For a photonic crystal fiber that has a core that consists of a single missing hole, the value for V_{PCF} below which the fiber is single mode can be derived to be π [38]. It can be calculated that all fibers that have approximately $d/P < 0.45$, where d is the hole diameter, are single mode for all wavelengths [47, 96]. For cores formed by more than a single missing hole the single mode criteria are $d/P < 0.25$ and $d/P < 0.15$ for three and seven missing holes, respectively [47].

The endlessly single mode behavior of the photonic crystal and microstructure fibers also allows for large mode area fiber that is single mode. Step index fiber becomes multimode when the core radius is increased [see Eq. (3.9)] since the refractive index difference between the core and the cladding cannot be decreased without limits. However, the single mode behavior of a photonic crystal fiber is independent of the core size and instead depends only on the cladding geometry. Thus large mode area fibers that are single mode can be constructed. Large mode area fibers are needed for high power delivery (for example in fiber lasers) since the nonlinear effects [which are inversely proportional to the mode area as in Eq. (3.5)] are smaller when the power density inside the fiber is low. The mode area of photonic crystal fibers is also limited by increasing propagation losses: if $V_{PCF} < 1$, the confinement of the mode is too weak and it leaks to the cladding

region [96]. Also, if the scale of the fiber is increased, the longitudinal modulations of the fiber (microbending, macrobending, and dielectric imperfections) can become too large compared to the wavelength [97, 98].

Since the first large mode area photonic crystal fiber [43], such fibers have become widely used in the development of photonic crystal fiber lasers [47]. Also, regarding nanojoule femtosecond pulses, large-core photonic crystal fibers are needed to avoid nonlinear processes which broaden a short pulse considerably affecting the dispersion compensation schemes [99]. Also, the single mode condition $d/P < 0.45$ was found not to be restrictive, since a fiber with $d/P = 0.5$ was shown to be single mode with a huge 600 μm^2 effective area [100].

Sometimes a small mode area is needed for large nonlinear effects (for example in supercontinuum generation or soliton formation). Small mode area is also achievable with photonic crystal fibers [44], and such fibers have been used extensively, some of the first experiments being introduced in Refs. [40, 101–103].

3.3 Dispersion properties

The dispersion properties of photonic crystal fibers can be designed more freely than those of the step index fibers. Probably the most revolutionary characteristic is that anomalous waveguide dispersion can be achieved with a single mode fiber [39], which is not possible with step index fibers. This property is important for soliton transmission, since solitons appear only with anomalous dispersion. Soliton transmission was observed at the wavelength 850 nm [104], which is not attainable with conventional fiber. Besides soliton propagation, anomalous dispersion at visible wavelengths, together with the low loss and small mode areas of photonic crystal fibers, allow for pulse compression and supercontinuum generation. Supercontinuum generation was experimentally verified for the first time in Ref. [40]. It has been demonstrated experimentally that the wavelength of zero group velocity can be engineered over a very wide range extending from 500 nm to 1.3 μm [42]. Since then, supercontinuum generation in photonic crystal fiber has been studied extensively both theoretically and experimentally [101–103, 105–117].

Photonic crystal fibers can also be designed to have flattened dispersion as a function of the wavelength [41, 118, 119]. This is needed for example for flat and wide band supercontinuum generation and in wavelength-division multiplexing communications systems for uniform response in the different channels. Flat, near zero dispersion over the wavelength range 1 μm-1.6 μm was experimentally demonstrated in Ref. [120]. Anomalous, flat dispersion was shown to lead to conversion of the wavelengths of a short pulse to both longer and shorter wavelengths [121].

Large negative values of the dispersion parameter [see Eq. (3.3)] are needed

in dispersion compensation and chirped pulse compression. This can also be achieved with photonic crystal fibers since the refractive index contrast between the core and the cladding can be increased by increasing the hole size [122–126].

3.4 Photonic band gap fibers

The most remarkable type of a photonic crystal fiber is the photonic band gap fiber which confines light into the core of the fiber by the photonic band gap effect. Thus light can be guided along, for example, air. This opens new prospects since, with air-core fiber, problems in optical fiber communication systems caused by light propagating in silica could be overcome.

True photonic band gap guidance [43] and light guidance in air [35] were first demonstrated in the end of the 90's. Theoretical analysis showed that the fiber exhibits, along with minimal nonlinearity, negligible dispersion, but the usable spectral range was shown to be small [127]. Hollow-core fibers also suffered from high loss, which was seen to result from coupling to lossy continuum or radiation modes [128, 129] and imperfections in the fiber [130]. However, low-loss hollow-core fiber has also been demonstrated [128].

3.5 Photonic crystal fiber applications

Hollow-core fibers have been used for applications where the fiber has been filled with gas. The nonlinear interaction between light and low-density media, such as gas or liquid, can be maximized in the core of a hollow-core fiber. Enhanced stimulated Raman scattering in hydrogen gas with energies two orders of magnitude lower than previously have been demonstrated [131, 132]. This wavelength conversion would allow for extending the wavelengths of solid-state diode-pumped lasers into new wavelength ranges. The detection of strongly absorbing (acetylene/hydrogen cyanide) and weakly absorbing (methane/ammonia) gases was demonstrated in Ref. [133]. Acetylene-filled hollow-core fiber could be used for absolute frequency-locking of diode lasers [132]. Hollow-core fiber has been also used to guide particles through the fiber by using the dipole force exerted by light [134].

Photonic crystal fibers can also be used in optical fiber sensing. For example curvature sensing has been demonstrated with multi-core fiber [135]. When the fiber is bend, the phase difference between the two cores changes, which can be detected from the output spectrum. Sensors for gases or liquids (for example detecting the concentration of pollutants in a gas) have also been explored [136].

Supercontinuum generated in a photonic crystal fiber is wider and flatter than could be previously achieved and it can be used in various spectroscopic experiments. It has been also used for optical coherence tomography to image biological

tissue [137]. There the broad bandwidth permits for record-breaking resolution and high penetration depth can be achieved for the infrared wavelengths. The high nonlinearity of a photonic crystal fiber can also be used to expand the spectral width of the frequency comb (evenly spaced frequency components of a pulse train) needed in frequency metrology [138, 139]. The high nonlinearity has also been used to make a regenerative all-optical switch, which exhibits amplitude restoration and pulse reshaping [140].

Photonic crystal fibers can be used as optical filters. A short-wavelength filter, which consists of a photonic crystal fiber with a depressed-index core but guides with total internal reflection, was fabricated [141]. The effective index of the cladding increases for decreasing wavelengths and finally exceeds that of the core. Light with wavelength shorter than that wavelength is not guided in the fiber. Optical filters and attenuators can also be realized by incorporating a doped region in the core allowing for grating writing and/or infusing cladding air-holes with active materials yielding tunable devices. Band rejection filters for flattening the gain of optical amplifiers were demonstrated using a long period grating written in the core. The grating induced coupling between the mode in the core and co-propagating cladding mode(s) due to phase matching which results in resonant loss at a certain wavelength [142]. The filters can be made tunable when active material is infused in the air holes. The cladding mode frequency is strongly affected when the refractive index of the active material is changed which affects the wavelength of the resonant loss [142]. Tunability can be achieved with, for example, temperature or electric field depending on the active material.

Nowadays, ytterbium and erbium doped photonic crystal fibers are extensively studied related to fiber amplifiers and lasers. Low pump power amplifiers can be realized since one can design the mode area of the photonic crystal fiber to be small and the index contrast between the core and the cladding to be large, in which case the light confinement is tight. Record breaking gain efficiencies have been demonstrated [143, 144]. On the other hand, high power amplifiers can be designed since the mode area can be designed to be large as well. Mode field area of 1000 μm^2 was used to amplify 10 ps pulses to 60 kW without nonlinearity induced spectral broadening [145]. The same approach has been used for femtosecond pulse amplification [146]. Similarly, photonic crystal fiber lasers with small mode area [147–150] and large mode area [145, 151–155] have been fabricated. Fiber laser made of polymer has also been demonstrated [156].

The high nonlinearity (due to small core size) and the dispersion properties of photonic crystal fibers have been used to achieve a tunable source in the wavelength range 1.06 μm-1.33 μm, which is difficult to realize by other means [157]. The high nonlinearity and anomalous dispersion allows for soliton self-frequency shift, which is used to tune the emitted wavelength.

3.6 Fabrication

The first photonic crystal and microstructure fibers were fabricated by drilling a hole in a macroscopic silica rod and milling the sides to form a hexagonal tube. This preform was drawn on a fiber drawing tower, cut to pieces which were stacked to form the periodic structure. This preform was then drawn again to microscopic scale [36]. The fabrication of photonic crystal fibers is done nowadays by stacking capillary tubes by hand to a bundle which is then drawn in a fiber drawing tower [34, 35, 40, 43, 158]. The stacking technique was already studied in the 70's in Bell laboratories [159].

Another way to fabricate photonic crystal fibers is extrusion. A polymer photonic crystal fiber fabricated by extrusion is introduced in Ref. [160]. The advantage of a polymer fiber over glass optical fiber is mechanical flexibility. Extrusion has been used also for chalgogenide glass [161] and glass fiber [162]. By extrusion, a more complicated microstructure can be fabricated to the preform than in the stacking procedure where the hexagonal symmetry is preferred.

Chapter 4

Numerical methods

The numerical methods used to study photonic crystals are numerous and they can roughly be divided in two major groups. One group of methods is used to calculate the band structure and eigenstates of the periodic system. The other group of methods studies the propagation of light in the structure, where the periodic nature of the system is not necessarily utilized. In this chapter, the methods used in this thesis are introduced.

4.1 Methods for solving eigenstates of periodic structures

In Publication I, a Fourier method was used to calculate band structures of nonlinear one-dimensional photonic crystals. In Publication III, a pseudo-spectral method was used to calculate band structures of two-dimensional photonic crystal slabs. It is a combination of plane wave and finite difference methods. In Publication II, the fully vectorial plane wave method developed in MIT and distributed as free software was used to calculate band structures for 2D photonic crystals, and in Publications IV and V to calculate the modes of the photonic crystal fibers.

4.1.1 Fourier method

The Fourier method for simulating linear photonic crystals is outlined in Ref. [163]. We have extended the method for nonlinear materials in Publication I. A schematic picture of a one-dimensional photonic crystal slab is shown in Fig. 4.1. The parameters that are needed in order to define a one-dimensional photonic crystal slab are the dielectric constants of the alternating layers ε_1 and ε_2, the thickness of one of the dielectric layers relative to the period, l/P, the height of the crystal scaled to the value of the period, h/P, and the type of the material surrounding the photonic crystal. The periodicity is in the y-direction. The one-dimensional periodic structure is assumed to be infinite in the x-direction, but limited in the

z-direction. The different areas are denoted by I, II, and III corresponding to the area above the crystal, the photonic crystal area, and the area below the crystal, respectively.

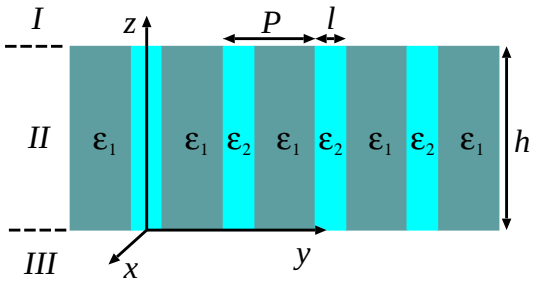

Figure 4.1: Schematic side view of a one-dimensional photonic crystal slab.

The material with ε_2 is taken to be Kerr-nonlinear and of thickness l. A Kerr-nonlinear material changes its properties depending on the intensity of light, $I(\mathbf{r})$, where the spatial dependence is denoted by vector $\mathbf{r}$. Thus, the dielectric constant of the nonlinear photonic crystal can be expressed as

$$\varepsilon_{NL}(\mathbf{r}) = \begin{cases} \varepsilon_1, & \text{for } -P/2 < y < -l/2,\ l/2 < y < P/2 \\ \varepsilon_2 + \chi^{(3)} I(\mathbf{r}), & \text{for } -l/2 \leq y \leq l/2 \end{cases} \tag{4.1}$$

where $\chi^{(3)}$ is the Kerr-coefficient. The field is assumed to be polarized according to

$$\mathbf{H}(\mathbf{r}) = H_x(y,z)\mathbf{e}_x, \tag{4.2}$$

where $\mathbf{e}_x$ is a unit vector in the x-direction. Therefore the electric field is lies in the y-z-plane

$$\mathbf{E}(\mathbf{r}) = E_y(y,z)\mathbf{e}_y + E_z(y,z)\mathbf{e}_z, \tag{4.3}$$

where $\mathbf{e}_y$ and $\mathbf{e}_z$ are unit vectors in the y- and z-directions, respectively. Maxwell's equations (2.11) and (2.12), in cgs units, can be written component-wise as

$$-\frac{i\omega\varepsilon_{NL}(y)}{c} E_y(y,z) = \partial_z H_x(y,z) \tag{4.4}$$

$$\partial_y H_x(y,z) = \frac{i\omega\varepsilon_{NL}(y)}{c} E_z(y,z) \tag{4.5}$$

$$\partial_y E_z(y,z) - \frac{i\omega}{c} H_x(y,z) = \partial_z E_y(y,z). \tag{4.6}$$

The electric field component $E_z(y,z)$ is solved from Eq. (4.5) and substituted in Eq. (4.6), which leads to the form

$$-\frac{i\omega}{c} H_x(y,z) + \frac{c}{i\omega}\partial_y \left(\frac{1}{\varepsilon_{NL}(y)} \partial_y H_x(y,z) \right) = \partial_z E_y(y,z). \tag{4.7}$$

The periodic field distributions are represented as Fourier-series

$$H_x(y,z) = \sum_n H_n(k_0,\omega)e^{\lambda z}e^{ik_n y}, \tag{4.8}$$

$$E_y(y,z) = \sum_n E_n(k_0,\omega)e^{\lambda z}e^{ik_n y}, \tag{4.9}$$

$$k_n = k + 2\pi n/P, \tag{4.10}$$

where k is the y-component of the wavevector. Exponential z-dependence is assumed and λ is a constant representing the z-dependence of the field components. The nonlinear dielectric constant and its inverse are expanded as Fourier-series

$$\varepsilon_{NL}(y) = \sum_n \varepsilon_n e^{i2\pi n/P} \tag{4.11}$$

$$\frac{1}{\varepsilon_{NL}(y)} = \sum_n \left[\frac{1}{\varepsilon}\right]_n e^{i2\pi n/P}. \tag{4.12}$$

The coefficients ε_n are found to be (see Appendix A)

$$\varepsilon_n = (\varepsilon_2 - \varepsilon_1)\frac{l}{P}\mathrm{sinc}\left(n\pi\frac{l}{P}\right) + \varepsilon_1\delta_{0,n} + \frac{l}{P}\sum_m \chi^{(3)} I_m \mathrm{sinc}\left[(m-n)\pi\frac{l}{P}\right], \tag{4.13}$$

where $\delta_{0,n}$ is the Kronecker delta and the I_m are the Fourier-coefficients of the intensity distribution

$$I(y) = \sum_n I_n e^{i2\pi n/P}. \tag{4.14}$$

The coefficients of the inverse dielectric function (4.12) are achieved by inverting the series (4.11).

The Maxwell's equations are transformed into a discrete form by substituting Eqs. (4.8)–(4.10) into Eqs. (4.4) and (4.7), multiplying by $e^{-ik_m y}$, and integrating from $-P/2$ to $P/2$. This leads to

$$-\frac{i\omega}{c}\sum_n E_n\varepsilon_{n-m} = \lambda\sum_n H_n\delta_{m-n} \tag{4.15}$$

$$-\frac{i\omega}{c}\sum_n H_n\delta_{m-n} - \frac{c}{i\omega}\sum_n H_n\left[\frac{1}{\varepsilon}\right]_{n-m} k_n k_m = \lambda\sum_n E_n\delta_{m-n}, \tag{4.16}$$

where the summations are truncated to $-N\ldots N$ components. The coefficients of the Fourier-series of the fields are denoted by vectors

$$H = [H_{-N},\ldots,H_0,\ldots,H_N]^T \tag{4.17}$$

$$E = [E_{-N}, \ldots, E_0, \ldots, E_N]^T \tag{4.18}$$

and Eqs. (4.15)-(4.16) are represented in matrix form as

$$\begin{bmatrix} 0 & -\varepsilon_{m-n} \\ -\delta_{m-n} - \tilde{k}_m \tilde{k}_n \left[\frac{1}{\varepsilon}\right]_{m-n} & 0 \end{bmatrix} \begin{bmatrix} H \\ E \end{bmatrix} = \tilde{\lambda} \begin{bmatrix} \delta_{m-n} & 0 \\ 0 & \delta_{m-n} \end{bmatrix} \begin{bmatrix} H \\ E \end{bmatrix}. \tag{4.19}$$

The variables k_n and λ are scaled according to $\tilde{k}_n = k_n c/(i\omega)$ and $\tilde{\lambda} = \lambda c/(i\omega)$. Equation (4.19) is a diagonal eigenvalue problem. From the eigenvalues, one can derive λ, which are the coefficients of the exponential z-dependence of the fields. The fields are written as

$$\begin{bmatrix} H \\ E \end{bmatrix} = \sum_{n=1}^{2(N+1)} C_n \mathbf{v}_n e^{\lambda_n z}, \tag{4.20}$$

where $\mathbf{v}_n$ denote the eigenvectors and λ_n denote the corresponding eigenvalues. The solution is (in matrix form)

$$\begin{bmatrix} H \\ E \end{bmatrix} = \begin{bmatrix} \mathbf{v}_1 e^{\lambda_1 z} & \ldots & \mathbf{v}_{2N+1} e^{\lambda_{2N+1} z} \end{bmatrix} \begin{bmatrix} C_1 \\ \ldots \\ C_{2N+1} \end{bmatrix} = \mathbf{MC}, \tag{4.21}$$

where the unknown coefficients C_n constitute a vector denoted by $\mathbf{C}$. The coefficients are determined from the boundary conditions: the tangential field components of $\mathbf{E}$ and $\mathbf{H}$ are demanded to be the same on both sides of the interfaces ($z = 0$ and $z = h$)

$$\begin{bmatrix} \mathbf{M}_{\mathrm{I}} & \mathbf{M}_{\mathrm{II}} & 0 \\ 0 & \mathbf{M}_{\mathrm{II}} & \mathbf{M}_{\mathrm{III}} \end{bmatrix} \begin{bmatrix} \mathbf{C}_{\mathrm{I}} \\ \mathbf{C}_{\mathrm{II}} \\ \mathbf{C}_{\mathrm{III}} \end{bmatrix} = 0, \tag{4.22}$$

where the subscripts denote the different areas as shown in Fig. 4.1. In the case of metallic boundaries the boundary conditions reduce to

$$\begin{bmatrix} E(z=0) \\ E(z=h) \end{bmatrix} = 0, \tag{4.23}$$

where taking only the electric field component into account is sufficient to solve the C_n.

The band structure of a photonic crystal is given by the dispersion relation $(\omega P/(2\pi c), kP/(2\pi))$, which is determined by solving Eqs. (4.19)-(4.22). These equations are considered for all combinations of $(\omega P/(2\pi c), kP/(2\pi))$, and the determinant of the interface conditions matrix (4.22) is calculated for each of the $(\omega P/(2\pi c), kP/(2\pi))$. Minima of the determinant of the interface conditions matrix correspond to the band structure points.

The band structure of a nonlinear photonic crystal is calculated in a manner somewhat similar to the self-consistent mean field approximation used to solve many body systems with interactions. Firstly, the field $[H, E]$ for the control plane wave with a specified frequency is determined assuming a linear material. The intensity distribution (4.14) is calculated using the E_z-component of the electric field, which is determined from Eq. (4.5). The E_z component is perpendicular to the direction of propagation and thus the longitudinal E_y component is several orders of magnitude smaller. The intensity distribution is normalized to have the same average energy at each step. The dielectric function for the next iteration step is acquired by substituting the Fourier-coefficients of the intensity distribution I_m to Eq. (4.13). In the next iteration step, the field $[H, E]$, the intensity distribution, and $\varepsilon_{NL}(y)$ are re-calculated for the same control plane wave frequency. The iteration is continued until the intensity distribution does not change anymore. The dielectric function obtained in the iterative process is used to calculate the band structure of the nonlinear photonic crystal under the influence of the control plane wave.

4.1.2 Pseudo-spectral method

The pseudo-spectral method for the calculation of the band structures of two-dimensional photonic crystal slabs with a finite thickness is introduced in (and presented here following) Ref. [164]. In the pseudo-spectral method, Maxwell's equations (in SI units) are transformed to a set of two matrix equations

$$\begin{bmatrix} 0 & \mathbf{A} \\ \mathbf{B} & 0 \end{bmatrix} \begin{bmatrix} E_x \\ E_y \\ H_x \\ H_y \end{bmatrix} = \partial_z \begin{bmatrix} E_x \\ E_y \\ H_x \\ H_y \end{bmatrix}, \tag{4.24}$$

where

$$\mathbf{A} = \begin{bmatrix} \partial_x \frac{1}{j\omega\varepsilon} \partial_y & -\partial_x \frac{1}{j\omega\varepsilon} \partial_x + j\omega\mu \\ \partial_y \frac{1}{j\omega\varepsilon} \partial_y - j\omega\mu & -\partial_y \frac{1}{j\omega\varepsilon} \partial_x \end{bmatrix} \tag{4.25}$$

$$\mathbf{B} = \begin{bmatrix} -\partial_x \frac{1}{j\omega\varepsilon} \partial_y & \partial_x \frac{1}{j\omega\varepsilon} \partial_x - j\omega\varepsilon \\ -\partial_y \frac{1}{j\omega\varepsilon} \partial_y + j\omega\varepsilon & \partial_y \frac{1}{j\omega\varepsilon} \partial_x \end{bmatrix} \tag{4.26}$$

and

$$\begin{bmatrix} 0 & 0 & \frac{1}{j\omega\varepsilon}\partial_y & -\frac{1}{j\omega\varepsilon}\partial_x \\ -\frac{1}{j\omega\varepsilon}\partial_y & \frac{1}{j\omega\varepsilon}\partial_x & 0 & 0 \end{bmatrix} \begin{bmatrix} E_x \\ E_y \\ H_x \\ H_y \end{bmatrix} = \begin{bmatrix} E_z \\ H_z \end{bmatrix}. \tag{4.27}$$

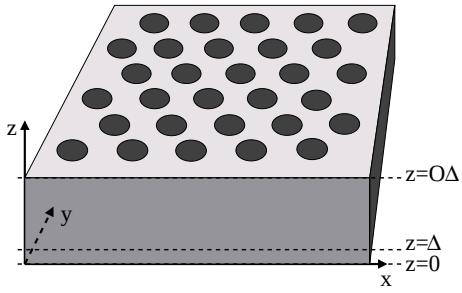

Figure 4.2: Geometry of the photonic crystal slab considered in the pseudo spectral method. The slab extends from $z = 0$ to $z = O\Delta$. The fields are defined at planes $z = o\Delta$.

The basic idea of the method is to discretize the field components in the z-direction and solve Eq. (4.24) by a finite difference scheme. Eq. (4.24) involves only the transversal components with respect to the z-direction and as they are solved in a plane, Eq. (4.24) can be used to obtain them in the z-direction. The z-components can then be solved from Eq. (4.27).

The fields are expanded as

$$\Psi(x, y, z) = \sum_{m,n} f_{m,n}(z) e^{i\mathbf{k}_{m,n}\cdot\mathbf{r}}, \tag{4.28}$$

where $f_{m,n}(z)$ are expansion coefficients. The system is divided in planes $z = o\Delta$ in the z-direction, where o is an integer. The slab extends from $z = 0$ to $z = O\Delta$ (see Fig. 4.2). The electric field components are defined on planes $o \pm 1/2$ and the magnetic field components on planes o and $o + 1$. The field ansatz (4.28) is substituted in Eq. (4.24) and it is transformed into the form

$$\mathbf{e}_{o-\frac{1}{2}} - \mathbf{e}_{o+\frac{1}{2}} + \Delta\mathbf{A}\mathbf{h}_o = 0 \tag{4.29}$$

$$\mathbf{h}_o - \mathbf{h}_{o+1} + \Delta\mathbf{B}_{o+\frac{1}{2}}\mathbf{e}_{o+\frac{1}{2}} = 0, \tag{4.30}$$

where the fields are represented by coefficient vectors $\mathbf{e}_o$ and $\mathbf{h}_o$ consisting of $f_{m,n}(z)$ at the plane $z = o$, and the matrices $\mathbf{A}$ and $\mathbf{B}$ are discrete. The fields outside the photonic crystal slab [at planes $z = (-1/2)\Delta$ and $z = (O + 1/2)\Delta$] are determined from

$$\Phi_l\mathbf{e}_{-1/2} - \mathbf{h}_0 = 0 \tag{4.31}$$

$$\mathbf{h}_O + \Phi_u\mathbf{e}_{O+1/2} = 0, \tag{4.32}$$

where Φ_u and Φ_l are boundary condition matrices that can be analytically solved by assuming the fields above and below the slab to be of the form

$$\Psi(x, y, z) = \sum_{m,n,o} \alpha_o f_{m,n,o} e^{\alpha_0 z} e^{i\mathbf{k}_{m,n}\cdot\mathbf{r}}. \tag{4.33}$$

The equations (4.29) and (4.30) are evaluated at each $z + o\Delta$-plane and all the unknown vectors $\mathbf{e}_o$ and $\mathbf{h}_o$ are collected into one vector $\mathbf{f}$ and all the multipliers into a matrix $\mathbf{M}$, which results in

$$\mathbf{Mf} = 0. \tag{4.34}$$

This equation is then solved by an iterative solver.

4.1.3 Fully vectorial plane wave method

The fully vectorial plane wave method is widely used in the study of photonic crystals. It was developed in MIT and is currently being distributed as free software called the MIT Photonic Bands. The method is explained in Ref. [165].

The fully vectorial plane wave method is based on the master equation (2.13) and its later form Eq. (2.25). The eigenstates [see Eq. (2.24)] are expanded in a plane wave basis

$$\mathbf{u_k}(\mathbf{r}) = \sum_{m=1}^{N} h_m e^{i \sum_j m_j \mathbf{G}_j \cdot \mathbf{r}}, \tag{4.35}$$

where $\mathbf{G}_j$ are the primitive reciprocal lattice vectors [unit components of $\mathbf{G}$ in Eq. (2.21)], $N = N_1 N_2 N_3$ is the number of basis vectors the system has been reduced to (the N_1, N_2, N_3 are the number of basis vectors in the three directions), and $m_j = -N_j/2 + 1, ..., N_j/2$. The eigenequation (2.25) is cast in a form of a matrix equation

$$\mathbf{Bh} = \left(\frac{\omega}{c}\right)^2 \mathbf{h}, \tag{4.36}$$

where $\mathbf{h}$ consists of the coefficients h_m and $\mathbf{B}$ represents the operator operating on $\mathbf{u_k}(\mathbf{r})$ in Eq. (2.25).

The primitive lattice vectors are $\mathbf{R}_i$ [unit components of Eq. (2.19)] and they satisfy $\mathbf{R}_i \cdot \mathbf{G}_j = 2\pi\delta_{i,j}$. Then the spatial field becomes

$$\mathbf{u_k}(\sum_k n_k \mathbf{R}_k/N_k) = \sum_{\{m_j\}} \mathbf{h}_{\{m_j\}} e^{i \sum_{j,k} m_j \mathbf{G}_j \cdot n_k \mathbf{R}_k/N_k} = \sum_{\{m_j\}} \mathbf{h}_{\{m_j\}} e^{2\pi \sum_j m_j n_j/N_j}, \tag{4.37}$$

where $n_k = 0, ..., N_{k-1}$ describe spatial coordinates on an $N_1 \times N_2 \times N_3$ grid. This equation is a three-dimensional discrete Fourier transform and thus the field in the spatial and wavevector spaces is related by a Fourier transform.

Equation (4.36) can be solved in the following way. The curls $[(i\mathbf{k}+\nabla)\times]$ [see Eq. (2.25)] are solved in the wavevector space, where they are replaced by $[(\mathbf{k} + \mathbf{G}_m)\times]$ and the multiplication by $[1/\varepsilon(\mathbf{r})]$ is performed in the spatial domain by taking the Fourier transform of $\mathbf{h}$, multiplying by $[1/\varepsilon(\mathbf{r})]$ and taking the inverse Fourier transform back to the wavevector space. Instead of solving the total matrix equation (4.36), iterative eigensolvers can be used to calculate only few smallest

eigenvalues and eigenvectors since often only the lowest energy eigenstates of the Maxwell's equations are needed.

4.2 Methods for studying the propagation of optical fields

In Publications II and III, the finite difference time-domain method, and in Publication V, the optical nonlinear Schrödinger equation, were used to study electromagnetic field propagation in time.

4.2.1 Finite difference time domain method

The finite difference time domain (FDTD) method is explained in Ref. [166]. The FDTD method starts from the Maxwell's equations, which were presented in cgs units in Eqs. (2.1)-(2.4). Here, the Eqs. (2.3) and (2.4) are presented in SI units (assuming linear and isotropic material and no free charges or currents)

$$\frac{\partial \mathbf{H}(\mathbf{r},t)}{\partial t} = -\frac{1}{\mu_0}\nabla \times \mathbf{E}(\mathbf{r},t) \tag{4.38}$$

$$\frac{\partial \mathbf{E}(\mathbf{r},t)}{\partial t} = \frac{1}{\varepsilon(\mathbf{r})}\nabla \times \mathbf{H}(\mathbf{r},t). \tag{4.39}$$

In the FDTD method, time and space are discretized and the values of the field components E_x, E_y, E_z, H_x, H_y, and H_z at the discretization points are denoted with indexes

$$u(i\Delta x,\, j\Delta y, k\Delta z, n\Delta t) = u^n_{i,j,k}, \tag{4.40}$$

where the Δx, Δy, Δz, Δt are the discrete increments in space and time, respectively, and the integers i, j, k define the point in space and n defines the point in time. The partial derivatives in the discretized system can be written as

$$\frac{\partial u}{\partial x}(i\Delta x,\, j\Delta y, k\Delta z, n\Delta t) = \frac{u^n_{i+1/2,j,k} - u^n_{i-1/2,j,k}}{\Delta x} \tag{4.41}$$

and correspondingly for the other variables.

Now the Maxwell's equations (4.38) and (4.39) are written component-wise. The electric field components are derived from Eq. (4.39)

$$\begin{aligned} E_x|^{n+1/2}_{i,j+1/2,k+1/2} =& E_x|^{n-1/2}_{i,j+1/2,k+1/2} + D_{i,j+1/2,k+1/2} \\ & \left(\frac{H_z|^n_{i,j+1/2,k+1/2} - H_z|^n_{i,j,k+1/2}}{\Delta y} \right. \\ & \left. - \frac{H_y|^n_{i,j+1/2,k+1/2} - H_y|^n_{i,j+1/2,k}}{\Delta z} \right) \end{aligned} \tag{4.42}$$

$$E_y|^{n+1/2}_{i-1/2,\,j+1,k+1/2} = E_y|^{n-1/2}_{i-1/2,\,j+1,k+1/2} + D_{i-1/2,\,j+1,k+1/2} \left(\frac{H_x|^n_{i-1/2,\,j+1,k+1} - H_x|^n_{i-1/2,\,j+1,k}}{\Delta z} - \frac{H_z|^n_{i,\,j+1,k+1/2} - H_z|^n_{i-1,\,j+1,k+1/2}}{\Delta x} \right) \tag{4.43}$$

$$E_z|^{n+1/2}_{i-1/2,\,j+1/2,k+1} = E_z|^{n-1/2}_{i-1/2,\,j+1/2,k+1} + D_{i-1/2,\,j+1/2,k+1} \left(\frac{H_y|^n_{i,\,j+1/2,k+1} - H_y|^n_{i-1,\,j+1/2,k+1}}{\Delta x} - \frac{H_x|^n_{i-1/2,\,j+1,k+1} - H_x|^n_{i-1/2,\,j+1,k+1}}{\Delta y} \right), \tag{4.44}$$

where the coefficients are

$$D_{i,\,j,k} = \frac{\Delta t}{\varepsilon_{i,\,j,k}}. \tag{4.45}$$

The magnetic field components are [from Eq. (4.38)]

$$H_x|^{n+1}_{i-1/2,\,j+1,k+1} = H_x|^n_{i-1/2,\,j+1,k+1} + \frac{\Delta t}{\mu_0} \left(\frac{E_y|^{n+1/2}_{i-1/2,\,j+1,k+3/2} - E_y|^{n+1/2}_{i-1/2,\,j+1,k+1/2}}{\Delta z} - \frac{E_z|^{n+1/2}_{i-1/2,\,j+3/2,k+1} - E_z|^{n+1/2}_{i-1/2,\,j+1/2,k+1}}{\Delta y} \right) \tag{4.46}$$

$$H_y|^{n+1}_{i,\,j+1/2,k+1} = H_y|^n_{i,\,j+1/2,k+1} + \frac{\Delta t}{\mu_0} \left(\frac{E_z|^{n+1/2}_{i+1/2,\,j+1/2,k+1} - E_z|^{n+1/2}_{i-1/2,\,j+1/2,k+1}}{\Delta x} - \frac{E_x|^{n+1/2}_{i,\,j+1/2,k+3/2} - E_x|^{n+1/2}_{i,\,j+1/2,k+1/2}}{\Delta z} \right) \tag{4.47}$$

$$H_z|^{n+1}_{i,\,j+1,k+1/2} = H_z|^n_{i,\,j+1,k+1/2} + \frac{\Delta t}{\mu_0} \left(\frac{E_x|^{n+1/2}_{i,\,j+3/2,k+1/2} - E_x|^{n+1/2}_{i,\,j+1/2,k+1/2}}{\Delta y} - \frac{E_y|^{n+1/2}_{i+1/2,\,j+1,k+1/2} - E_y|^{n+1/2}_{i-1/2,\,j+1,k+1/2}}{\Delta x} \right). \tag{4.48}$$

The magnetic field components are defined at time steps n and the electric field components at time steps $(n + 1/2)$, where $n = 1, 2, ..., N$. It can be seen from

Eqs. (4.42)-(4.44) that the electric field components at time $(n + 1/2)$ are completely defined by the previous value of the corresponding electric field component and the magnetic field values at time n. Also the magnetic field components at time step $n + 1$ [see Eqs. (4.46)-(4.48)] are defined by the value of the magnetic field at the previous time step and the values of the electric fields at time $n + 1/2$. Thus the field values need not to be defined at the same time steps. Similarly, the field components are defined at different points of the discretized space.

The Eqs. (4.42)-(4.48) are used to propagate the fields in time. Care has to be taken in order to assure stability of the method. It has been shown that the time step must be bounded

$$\Delta t \leq c \left[\frac{1}{(\Delta x)^2} + \frac{1}{(\Delta y)^2} + \frac{1}{(\Delta z)^2} \right]^{-\frac{1}{2}}, \tag{4.49}$$

for the FDTD method to be stable [166].

Obviously the FDTD method can be used to describe electromagnetic fields in a finite area in space. However, problems in unbounded regions can be simulated by including absorbing boundary conditions to the edges of the calculational domain. The best performance is attained by using the perfectly matched layer (PML) boundary conditions where the reflection from the boundaries back to the calculational region is a great deal smaller than while using other types of absorbing boundary conditions.

In the PML boundary conditions, a PML medium is taken to surround the calculational domain. The PML medium is designed in such a way that the reflection in the boundary between the calculational domain and the PML medium is zero. The reflection at the interface of the two media depends on the wave impedances of the media: when the wave impedances are equal, the reflection at normal incidence is zero. The wave impedance is defined as

$$Z = \sqrt{\frac{\mu(1 + \sigma^*/j\omega\mu)}{\varepsilon(1 + \sigma/j\omega\varepsilon)}}, \tag{4.50}$$

where σ^* is a parameter characterizing magnetic loss. For nonconducting and lossless medium, the wave impedance is $Z = \sqrt{\mu/\epsilon}$. The wave impedances of the PML medium and the calculational area are equal if $\varepsilon_{PML} = \varepsilon$, $\mu_{PML} = \mu$, and $\sigma^*_{PML} = \sigma_{PML}\mu/\varepsilon$. This defines the PML medium. Allowing anisotropic conductivities σ_x, σ_y, σ_y, and magnetic losses σ^*_x, σ^*_y, σ^*_z, the impedance matching can be realized for all incoming angles. The wave transmitted to the PML medium propagates exactly at the same speed and to the same direction as in the calculational region, but decays exponentially in the direction normal to the interface.

In addition to simulating the propagation of the electromagnetic fields, the finite difference time-domain method can also be used to solve the eigenstates and band structures of photonic crystals [167].

4.2.2 Split-step Fourier method

The optical nonlinear Schrödinger equation describes the evolution of the slowly varying envelope A of an optical pulse in a fiber (see Section 3.1 and Appendix B)

$$\begin{aligned}\frac{\partial A}{\partial z} = &-\sum_{n=1}^{M}\frac{i^{n+1}}{n!}\beta_n\frac{\partial^n A}{\partial T^n} - \frac{\alpha A}{2}\\ &+ i\gamma\left(1+\frac{i}{\omega_0}\frac{\partial}{\partial T}\right)A\int_{-\infty}^{\infty}R(T')|A(z,T-T')|^2dT',\end{aligned} \tag{4.51}$$

and it can be solved by the split-step Fourier method, which is explained in Ref. [94]. In the split-step Fourier method, the optical nonlinear Schrödinger equation is cast into the form

$$\frac{\partial A}{\partial z} = (\hat{D}+\hat{N})A, \tag{4.52}$$

where the dispersion and nonlinear operators are

$$\hat{D} = -\sum_{n=1}^{M}\frac{i^{n+1}}{n!}\beta_n\frac{\partial^n}{\partial T^n} - \frac{\alpha}{2} \tag{4.53}$$

$$\hat{N} = i\gamma\left(1+\frac{i}{\omega_0}\frac{\partial}{\partial T}\right)\int_{-\infty}^{\infty}R(T')|A(z,T-T')|^2dT', \tag{4.54}$$

respectively. From Eq. (4.52) it is seen that A can be propagated a distance h by

$$A(z+h,T) \approx e^{h\hat{D}}e^{h\hat{N}}A(z,T), \tag{4.55}$$

where the equality is approximate since the operators $\hat{N}$ and $\hat{D}$ do not commute. A more accurate form of Eq. (4.55) is

$$A(z+h,T) \approx e^{\frac{h}{2}\hat{D}}e^{\int_z^{z+h}\hat{N}(z')dz'}e^{\frac{h}{2}\hat{D}}A(z,T). \tag{4.56}$$

What makes this method very fast is that the dispersion operator can executed in the Fourier-domain

$$e^{\frac{h}{2}\hat{D}}A(z,T) = \{F^{-1}e^{\frac{h}{2}\hat{D}(i\omega)}F\}A(z,T) \tag{4.57}$$

where F denotes Fourier transform and the operator $\hat{D}(i\omega)$ can be achieved by replacing in Eq. (4.53) the time derivatives $\partial/\partial T$ by $i\omega$. Eq. (4.57) is merely a multiplication and the Fourier transforms can be calculated by the fast Fourier transform method.

The nonlinear operator can be calculated iteratively using

$$\int_z^{z+h} \hat{N}(z')dz' \approx \frac{h}{2}[\hat{N}(z) + \hat{N}(z+h)]. \tag{4.58}$$

In the first step, $\hat{N}(z+h)$ is replaced by $\hat{N}(z)$, and $A(z+h, T)$ is calculated from Eq. (4.56). This value of $A(z+h, T)$ is used to calculate $\hat{N}(z+h)$ from Eq. (4.54). This procedure is repeated a few times.

Chapter 5

Results

In this thesis, various optical components for telecommunications applications are studied. The results are summarized in this chapter. All-optical switching using one-dimensional photonic crystal slabs made of nonlinear material is the subject of Publication I. Coupling between two parallel waveguides in two-dimensional photonic crystals is studied in Publication II. Guiding of light in two-dimensional photonic crystal slabs using material on top/below the slab is studied in Publication III as a three-dimensional problem. Dispersion compensation using a photonic crystal fiber is studied in Publication IV. Short pulse amplification in high-gain efficiency photonic crystal fiber amplifiers is investigated in Publication V.

5.1 All-optical switching

One-dimensional photonic crystals are periodic in one direction only, and thus they have a band gap for light traveling in that direction. In Publication I, one-dimensional photonic crystals consisting of nonlinear materials were studied. Kerr-nonlinear materials change their refractive index n_{NL} depending on light intensity inside the material

$$n_{NL}^2(\mathbf{r}) = \varepsilon_{NL}(\mathbf{r}) = \varepsilon + \chi^{(3)} I(\mathbf{r}), \tag{5.1}$$

where $\chi^{(3)}$ is the Kerr-coefficient of the nonlinear material and $I(\mathbf{r})$ describes the local intensity distribution. One of the materials constituting the one-dimensional photonic crystal is taken to be Kerr-nonlinear and the refractive index of that material changes as a function of what is the light intensity inside the photonic crystal according to Eq. (5.1). When the refractive index of the material changes, also the band structure of the photonic crystal changes, because it is dependent of the refractive indices of the materials. Using this property, the nonlinear one-dimensional photonic crystal can be used as an all-optical switch [60, 61, 63, 64].

With this switch, one can block or let through a probe signal by using a control signal, with which the band gap of the photonic crystal is dynamically changed.

All-optical switching using a nonlinear photonic crystal is demonstrated in Fig. 5.1. The band structure of the one-dimensional photonic crystal when there is no light inside the structure is shown in the upper part of the figure. The probe pulse has its frequency in one of the band gaps of the photonic crystal and is thus reflected. When a control pulse is traveling through the photonic crystal, it changes the refractive index of the nonlinear material. Then the band structure of the photonic crystal changes also as is shown in the lower part of the figure. Now, the frequency of the probe pulse is not in the band gap anymore and thus it can be transmitted through the photonic crystal.

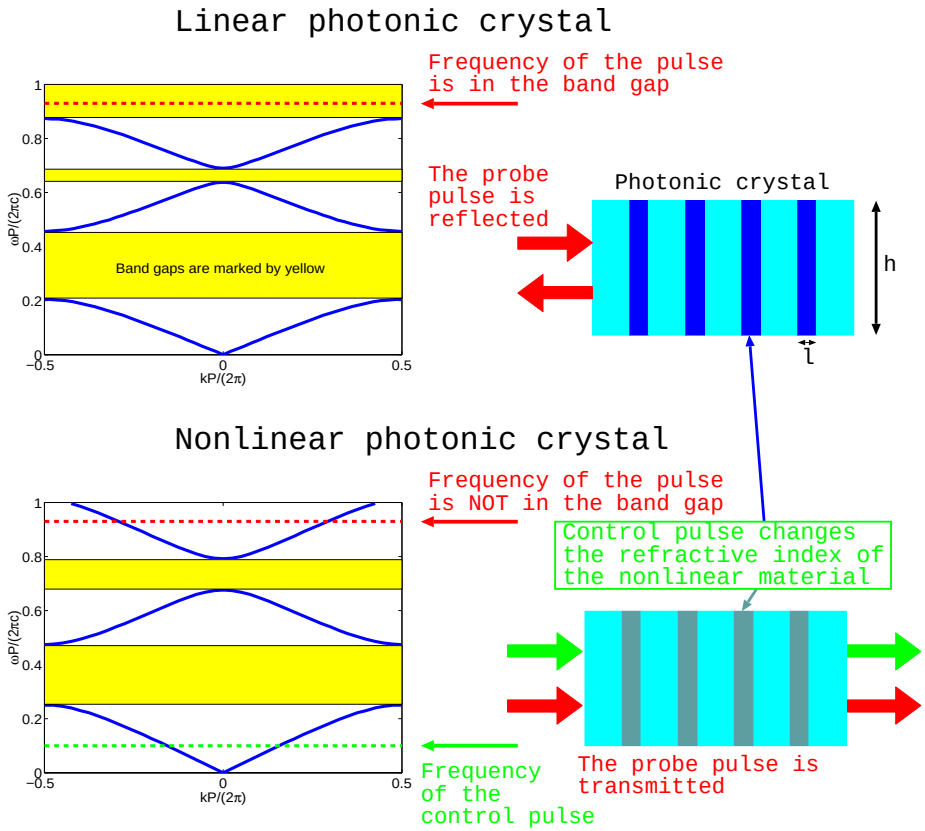

Figure 5.1: Upper part of the figure: band structure of the photonic crystal when there is no induced nonlinearity. The band gaps are denoted by yellow. The frequency of the probe pulse (denoted by red) is in the band gap. Lower part of the figure: band structure of the nonlinear photonic crystal when a control pulse has changed the refractive index of the nonlinear material. There exists a solution for the probe pulse frequency and thus the probe pulse can be transmitted through the crystal.

The band structures in Fig. 5.1 are calculated with the Fourier-method explained in Section 4.1.1. The parameter values of the photonic crystal are dielectric constants $\varepsilon_1 = 1$, $\varepsilon_2 = 13$, width of the nonlinear layer $l = 0.2\ P$, the height of the crystal $h = 0.4\ P$, the Kerr coefficient $\chi^{(3)} = -0.04$, and the intensity of the pulse $I = 2$ kW/cm^2. The material on top and below the photonic crystal is taken to be metal, because a metal coating reflects light with infrared wavelength and thus prevents the leakage. The number of Fourier components in the calculation was $N = 100$.

To estimate how an actual all-optical switch works, GaAs is used as the nonlinear material. The Kerr coefficient and the dielectric constant for GaAs are $\chi^{(3)} = -0.04$ (for the wavelength 0.84 μm) [168] and $\varepsilon = 13$, respectively. The change in the band structure shown in Fig. 5.1 requires that intensity of the control pulse is of the order of 2 kW/cm^2. However, a smaller intensity of 1 kW/cm^2 is enough to perform the optical switching function. In that case the change of the band edge is $\Delta\omega P/(2\pi c) = 0.92 - 0.87 = 0.05$. The probe pulse frequency $\omega P/2\pi c = 0.9$ is in the center of the switching range in order to avoid cut off at low or high frequencies. the probe pulse wavelength is $\lambda = 1.55\ \mu$m, which is the main frequency used in optical telecommunications. Thus the period of the photonic crystal is $P = 0.9 \times 1.55\ \mu\text{m} = 1.4\ \mu$m. The shortest pulse that could be switched with this all-optical switch is $3 \cdot 10^{-14}$ s, because shorter pulses have too large frequency ranges. If the amplitude of the control pulse is larger, even shorter pulses can be managed.

In order to show how the amplitude or intensity of the control pulse affects the nonlinear photonic crystal, band structures corresponding to various control pulse amplitudes are shown in Fig. 5.2. The parameter values of the photonic crystal geometry are the same than reported above, only the value of $\chi^{(3)}$ is taken to be 0.01. The corresponding dielectric functions and intensity distributions inside the photonic crystal are shown in Fig. 5.3. The simulation method is stable for nonlinear change in ε_2 up to $\varepsilon_{NL} = 2.5 \times \varepsilon_2$ for this particular crystal geometry and number of Fourier-coefficients N. The method is robust in describing the nonlinearity and in theory no restrictions for the magnitude of the nonlinearity are found. Larger nonlinearities can be simulated by increasing N. However, in practice limitations are set by computational time. The straight bands in Fig. 5.2 correspond to the k_z-modes. The height h determines which modes can exist in the z-direction, i.e., having a wavevector k_z. The amount of these modes is naturally increasing as h increases. Thus a small h value has to be chosen in order to have no k_z-modes in the region of the lowest bands.

In Publication I, the band structures of one-dimensional photonic crystal slabs incorporating nonlinear materials were calculated. Previous work regarding nonlinear one-dimensional photonic crystals has mainly concerned pulse propagation and dynamics in the structure. This work exposes a complementary view on the problem: the eigenmodes of the system. Also, the height of the photonic crystal

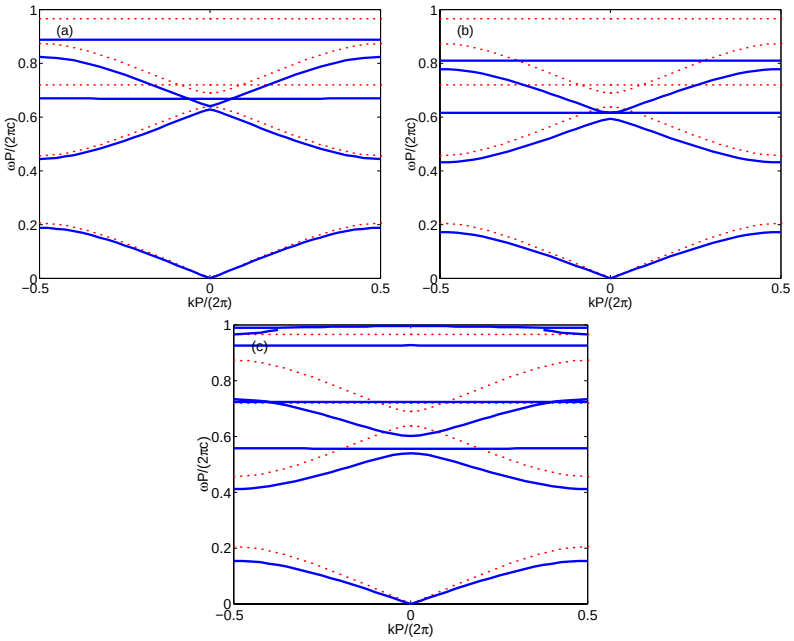

Figure 5.2: Band structures of a nonlinear photonic crystal with $\chi^{(3)} = 0.01$ (solid blue curves) and the corresponding linear photonic crystal (dotted red curves) for different amplitude values of the control pulse: (a) $A = 20$, (b) $A = 30$, and (c) $A = 40$.

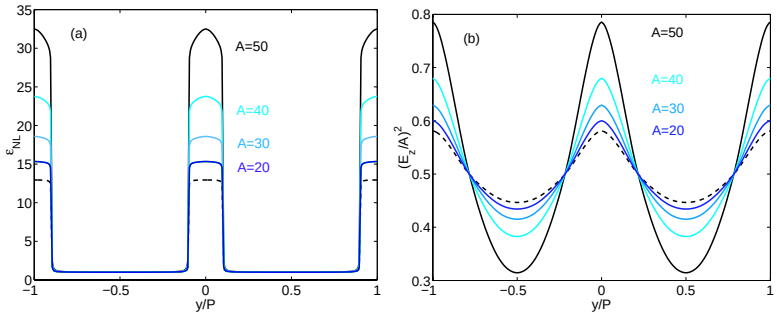

Figure 5.3: (a) The dielectric function $\varepsilon_{NL}(y)$ and (b) the intensity distribution at $z = 0$ of the linear photonic crystal (dashed curve) and that of the corresponding nonlinear crystal (solid curves) with $\chi^{(3)} = 0.01$ and when a plane wave with amplitude A is applied. Compare to Fig. 5.2.

slab is taken into account, and the problem is treated two-dimensionally.

5.2 Decoupling between two parallel waveguides

In Publication II, coupling between two parallel waveguides in a two-dimensional photonic crystal was studied. The coupling between waveguides is important in, e.g., directional waveguide couplers [169–173]. On the other hand, in integrated optical circuits cross-talk between two adjacent channels should be minimized [171, 174, 175]. We consider a specific geometry: a square lattice of dielectric rods in air (see Fig. 5.4). The distance of the two waveguides is varied (1-7 rows of rods between the waveguides are considered). The band structures of the systems are calculated with the fully vectorial plane wave method explained in Section 4.1.3.

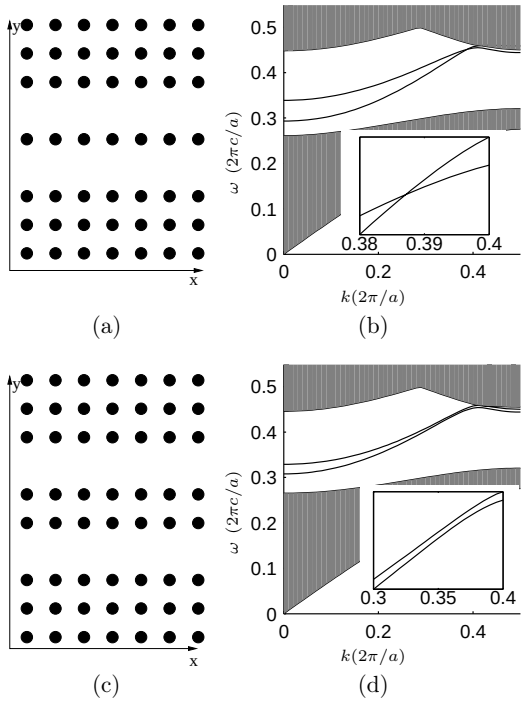

Figure 5.4: Geometries and band structures for one [(a) and (b)] and two [(c) and (d)] rows of dielectric rods between two parallel waveguides. The refractive index of the rods is 3, radius of the rods is $0.2P$, and the period of the lattice is $P = 512$ nm.

The studied geometries support two eigenmodes: even and odd with respect to the symmetry line between the waveguides. Any signal traveling in the waveguides can be represented as a superposition of these eigenmodes

$$\Psi(x, y, t) = \psi_E(x, y, t) \exp(ik_E x) + \psi_O(x, y, t) \exp(ik_O x), \qquad (5.2)$$

where ψ_E and ψ_O are the even and odd eigenmodes, and k_E and k_O are the

wavevectors of the even and odd modes, respectively. This means that the signal periodically oscillates between the waveguides. The period of this oscillation is

$$\kappa = \frac{2\pi}{|k_O - k_E|}. \tag{5.3}$$

The bands representing these modes were found to cross when there was an odd amount of rods between the waveguides [see Fig. 5.4 (b)]. The bands did not cross when there was en even number of rods between the waveguides [see Fig. 5.4 (d)]. At the point where the bands cross, the waveguides become decoupled. This can be seen from Eq. (5.3) as κ becomes infinite at the point where $k_O = k_E$. Thus, one can conclude that the waveguides become decoupled for certain frequencies of light when there is an odd amount of rods between the waveguides. Earlier work on the subject reported in the literature considered only an even number of rods between the waveguides and thus did not demonstrate the decoupling phenomenon.

This finding can be explained by taking a look at the mode distributions of the eigenmodes. The E_z and H_y components of the odd eigenmode have a node in the symmetry plane of the structure. The parity of the H_x component is the opposite of the parities of the E_z and H_y components. The symmetry line between the waveguides is in air if there is an even number of rods between the waveguides, whereas it crosses dielectric rods if there is an odd number of rods between the waveguides. Also, it is known that the larger the dielectric constant, the smaller the energy of an electromagnetic mode. From the modes of the structure it can be seen that the relative power of H_y as compared to that of H_x increases with increasing values of the wave vector. Thus, at small k, the effective parity of the odd mode is determined by H_x. Then the energy of the mode is small, because H_x has a maximum at the symmetry line, where the dielectric constant is high. At large k, the effective parity is determined by H_y, which has a node in the symmetry line and thus the odd mode has higher energy. Thus the energy of the odd mode is strongly increased as a function of k and crosses the band of the even mode. When there is an even number of rods between the waveguides, the node of the odd eigenmode is in air and the effective parity does not have such an effect to the energies of the eigenmodes.

5.3 Guiding and reflecting light with boundary material

In Publication III, thin photonic crystal slabs were studied. In a photonic crystal slab, light is confined in a plane by the photonic crystal and in the third direction by average refractive index difference [49, 176–180]. In our study, the materials on top/below the slab were changed. The half-spaces above and below the slab are called boundary materials. It was found that the band structure of the

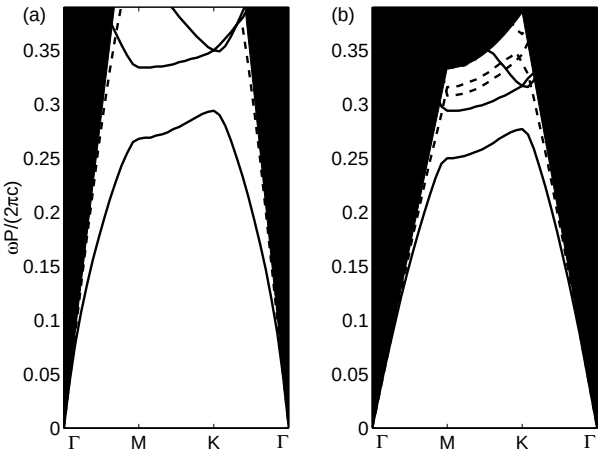

Figure 5.5: Band structures of a two-dimensional photonic crystal slab with triangular lattice of air holes. The geometry of the photonic crystal slabs is the same in (a) and (b). Only the material on top/below the slab, denoted by ε_b, is different. In (a) $\varepsilon_b = 1$ and in (b) $\varepsilon_b = 3$. The radius of the holes in the photonic crystal slab is $r/P = 0.24$ and the height of the slab is $h/P = 0.3$ with respect to the period P. Solid curves denote even modes, dashed curves denote odd modes and black areas are above the light lines for the boundary material in question.

photonic crystal slab changes depending on the boundary material, as is evident from Fig. 5.5. The band structures were calculated using the pseudo-spectral method introduced in Section 4.1.2.

The band gaps in Fig. 5.5 (a) and (b) are very different. This effect can be utilized in waveguiding. Usually waveguides in two-dimensional photonic crystal slabs are realized by line defects: for example missing rows of holes. Instead of a line defect, waveguiding can be acquired by patterning the slab by a boundary material as is demonstrated in Fig. 5.6. The photonic crystal slab is defectless, and the waveguide is realized simply by the effect of the boundary material. In this case, the frequency of the light traveling in the waveguide is in the band gap of the slab when it is uncovered, but not in the band gap of the covered slab. Thus, light can be transmitted in the covered region, but cannot be transmitted in the uncovered region. This means that the light follows the covered region, i.e., the waveguide.

More specifically, in Fig. 5.5 (a), the frequencies around $\omega P/(2\pi c) = 0.3$ fall into the band gap for even modes, but in Fig. 5.5 (b) there exists a mode at the M-point for the frequency $\omega P/(2\pi c) = 0.2937$. From this it can be calculated that if the waveguide is designed for the wavelength $\lambda = 1500$ nm, the period of the photonic crystal is $P = 450$ nm. A waveguide with a width $2P$ was studied and it was found that it transmits 40% more compared to the conventional waveguide

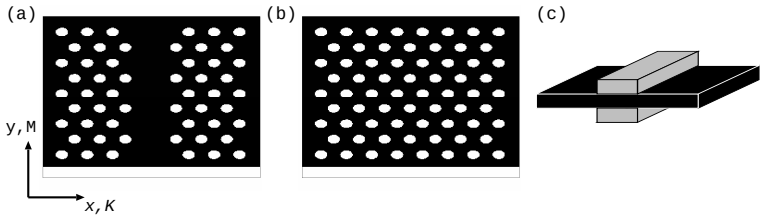

Figure 5.6: (a) Conventional waveguide in a photonic crystal slab: a line defect. (b) Guiding by boundary material is achieved in a defectless slab. (c) The guiding effect is introduced by the boundary material, which is patterned on top/below the photonic crystal slab. The boundary material changes the band structure of the slab and light is guided along the covered regions.

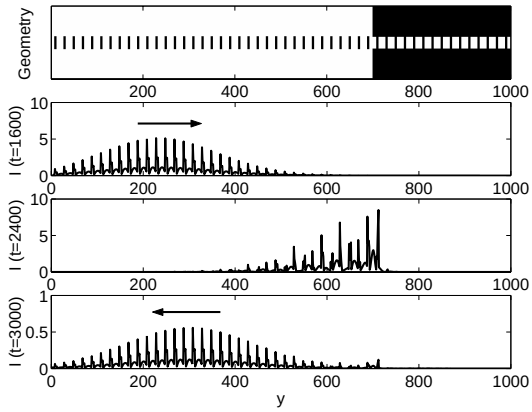

Figure 5.7: Cross section of the 1D photonic crystal slab is shown in the up-most part of the figure. The slab is uncovered until $y < 700$ and covered after that. In the lower part of the figure, the intensity of the pulse propagating along the slab is shown at different time steps. It can be seen that the pulse propagates along the slab until it is incident on the point where the boundary material suddenly changes. At that point the pulse is reflected.

shown in Fig. 5.6 (a). However, for some cases, the waveguiding was shown to result from average refractive index difference rather than the band gap difference.

The same phenomenon can be used in context with one-dimensional photonic crystal slabs. This is illustrated in Fig. 5.7. In the considered case, the pulse has such a frequency that it is in the band gap of the covered photonic crystal slab, but not of the uncovered slab. Thus the pulse can propagate along the photonic crystal slab when it is uncovered, but at the point where the slab is covered, the pulse reflects as it no longer can propagate along the covered slab.

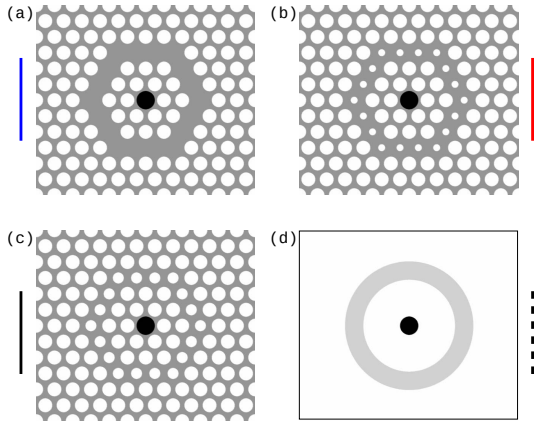

Figure 5.8: The studied fiber geometries have a defect ring in the cladding. The radius of the cladding air holes is $r = 0.38P$ and of the defect ring air holes $r = 0$ in (a), $r = 0.19P$ in (b), and $r = 0.3P$ in (c). The geometries are compared to corresponding average index dual-core fibers (d).

5.4 Dispersion compensation with photonic crystal and dual-core fibers

In Publication IV, photonic crystal fiber geometries were optimized in order to achieve large negative dispersion and large mode area simultaneously. This is usually contradictory since large dispersion fibers have small mode areas. Large negative dispersion fibers are used for dispersion compensation and pulse compression. Dispersion compensating fibers include photonic crystal fibers [122–126, 181, 182], dual-core fibers [183–186], Bragg fibers [187, 188], and higher-order mode fibers [189–192]. Dispersion compensation is required because standard single mode fiber has dispersion of 10-20 ps/(nm km) for the wavelengths around 1.55 μm. Pulse compression is needed in high power fiber amplifiers and lasers, where the pulse is first stretched, then amplified, and finally compressed. Large mode area fiber is especially needed in this scheme since nonlinear effects can destroy the laser operation.

We studied the so called dual-core geometries with a defect ring in the cladding. The studied geometries are shown in Fig. 5.8. The core refractive index for the three geometries was varied between $r_{core} = 1.5 \ldots 2.8$. All these geometries were compared to the corresponding dual-core fibers having the same average refractive index in the cladding and the defect ring.

The dispersion of the dual-core fibers is high since at a specific wavelength the eigenmode of the fiber changes from being confined in the core to being confined in the defect ring (see Fig. 5.9). At this wavelength, the effective index of the

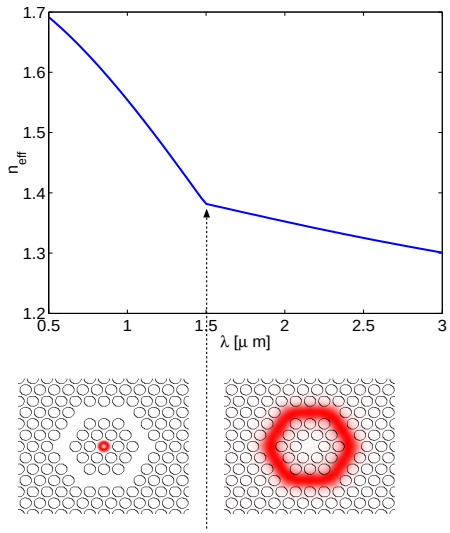

Figure 5.9: The effective index n_{eff} changes abruptly at the wavelength where the mode distribution changes from the core to the cladding.

mode $n_{eff} = \beta/k$ changes suddenly and because the dispersion is proportional to the derivative of the effective index

$$D = -\frac{\lambda}{c}\frac{\mathrm{d}^2 n_{\mathrm{eff}}}{\mathrm{d}\lambda^2}, \tag{5.4}$$

dispersion at this wavelength is very large.

The studied fibers were multimode and the studied mode is the third eigenmode. The values of the dispersion parameter for the studied geometry are shown in Fig. 5.10 (a) and the corresponding effective areas are shown in Fig. 5.10 (b). The effective areas are calculated from Eq. (3.6) and they correspond to the mode distribution that is confined to the defect ring. The obtained dispersion and effective area values are large compared to previous studies in the literature considering dispersion compensating photonic crystal fibers.

5.5 Pulse propagation in photonic crystal fiber amplifiers

In Publication V, short pulse propagation in high-gain efficiency photonic crystal fiber amplifiers [143, 144, 150, 193] was studied using the optical nonlinear Schrödinger equation [see Eq. (3.1)]. In high-gain efficiency fiber amplifiers, the overlap between the light distribution and the doped area of the fiber is maximized, and thus they usually have small mode areas. Photonic crystal fibers with small mode areas have relatively large dispersion and nonlinearity, and these parameters also depend strongly on the wavelength [194]. The wavelength dependence

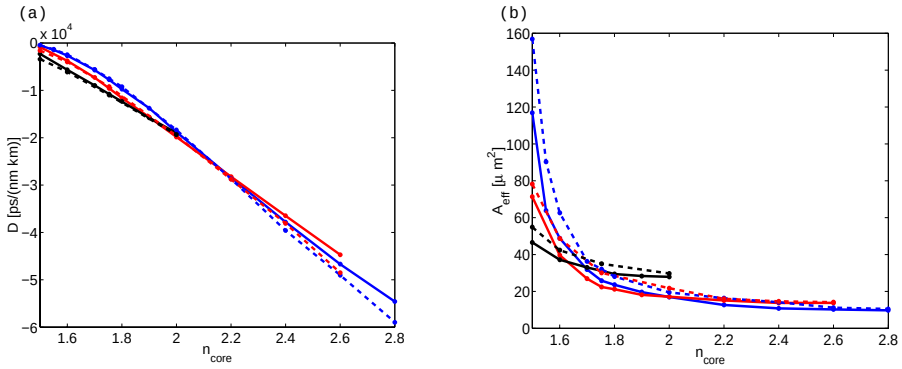

Figure 5.10: The dispersion parameters and effective areas for the different geometries of Fig. 5.8 as a function of the core refractive index. The color coding is as indicated in Fig. 5.8 and the dashed lines shown the values for the corresponding dual-core fibers.

of the fiber parameters (gain, dispersion and nonlinearity) was included in the simulations and the effect to the pulse quality was investigated.

We considered photonic crystal fiber geometries with hole diameter to period ratios $d/P = 0.2, 0.3, 0.4, 0.5, 0.6$ and periods $P = 2, 3, 4, 5, 6$ μm. The 200 fs pulses were propagated 10 cm along these photonic crystal fiber amplifiers. The propagation distance is short compared to the actual amplifier lengths, which can be several meters. The simulations for the different fiber geometries were performed twice: firstly with wavelength dependent parameters for dispersion β, nonlinearity γ, and gain, and secondly with keeping these parameters constant. The parameter values were calculated using the fully vectorial plane wave method [165] introduced in Section 4.1.3. The pulse propagation was calculated using the split-step Fourier method presented in Section 4.2.2.

The results for one fiber geometry are shown in Fig. 5.11. One can see that the wavelength dependence of the parameters affects the pulses so that the self-steepening of the pulse is reduced, and the spectrum and chirp become asymmetric. The asymmetric chirping may influence the dispersion compensation and pulse compression schemes. In general, the pulses broaden less both temporally and spectrally when the wavelength dependence of the parameters is taken into account. This is illustrated in Fig. 5.12 where the time-bandwidth products for the pulses after propagating in fibers with different geometries are shown. Time bandwidth product is the product of the temporal and spectral full-widths at half-maximum. The fact that the pulses broaden less when the wavelength dependence of the parameters is included in the simulation indicates that the wavelength dependence of the nonlinearity counteracts the dispersion of the fiber.

In order to compare the relative significance of including the wavelength dependence of the different fiber parameters, we performed two additional sets of

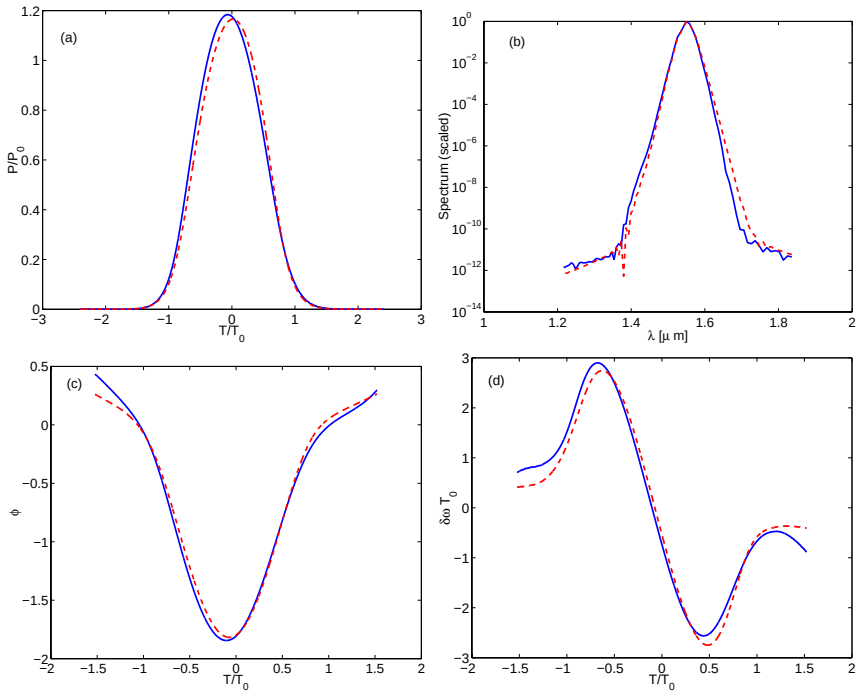

Figure 5.11: (a) Pulse shape, (b) spectrum, (c) phase, and (d) chirp for the fiber geometry of $d/P = 0.3$ and $P = 3$ μm. Blue curves represent the simulation with wavelength dependent parameters $[g(\lambda), \gamma(\lambda), \beta_m(\lambda)]$ and red dashed curves with constant parameter values for g, γ, β_m.

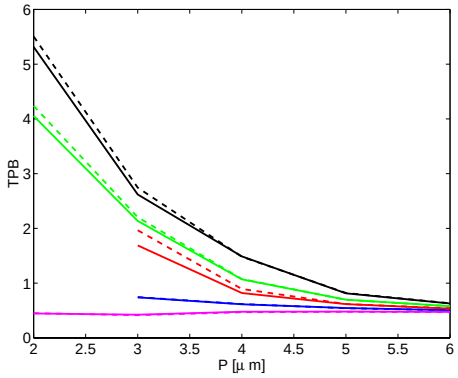

Figure 5.12: Time-bandwidth product of the pulses for the different fiber geometries: $d/P = 0.2$ (magenta curves), $d/P = 0.3$ (blue curves), $d/P = 0.4$ (red curves), $d/P = 0.5$ (green curves), and $d/P = 0.6$ (black curves) as a function of the period P. Solid curves represent the simulations for which the wavelength dependence of g, γ, and β_m is taken into account. Dashed curves represent the simulations where these parameters have constant values.

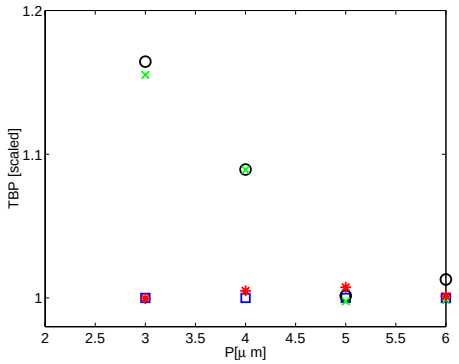

Figure 5.13: Time-bandwidth products (TBP) for four different sets of simulations: all parameters wavelength dependent (blue squares), dispersion constants approximated with constant values (red stars), all parameters constant (black circles), and only gain wavelength dependent (green crosses). The considered fiber geometries are $d/P = 0.4$ and $P = 3, 4, 5, 6\ \mu m$. The TBP values are scaled to the results of those simulations where all parameters are wavelength dependent for the corresponding fiber geometry.

pulse propagation simulations. Firstly, the dispersion parameters were approximated with constant values, and secondly, only gain was taken to be wavelength dependent. The time-bandwidth products are shown in Fig. 5.13, where it can be seen that the simulations with all parameters wavelength dependent (blue squares) and with dispersion parameters approximated with constant values (red stars) are similar. Also, the simulations with all parameters constant (black circles) and only gain wavelength dependent (green crosses) are similar. Thus, it can be concluded that the wavelength dependence of the nonlinearity has the most significant impact to the pulse characteristics as compared to the effect of the wavelength dependence of dispersion or gain. Thus, while studying pulse propagation, the dispersion and gain parameters could be approximated by constant values for some fiber geometries. However, when the spectral broadening of the pulse is strong, the wavelength dependence of all fiber parameters has to be included in the simulations.

Chapter 6

Conclusions

In this thesis, the properties of photonic crystals were studied and new components for optical telecommunications were proposed. The considered photonic crystal configurations were the following: nonlinear one-dimensional photonic crystal slabs, two-dimensional photonic crystals, thin two-dimensional photonic crystal slabs, and photonic crystal fibers. In each study, a different approach and thus different simulation methods had to be used.

One-dimensional photonic crystal slabs incorporating a Kerr-nonlinear material were investigated. The refractive index of the Kerr-nonlinear material changes as a function of the light intensity inside the material. We calculated the band structures of the photonic crystals while taking into account the nonlinearity of the material. The band gap of the photonic crystal was shown to change as a function of light intensity inside it. The performance of the nonlinear one-dimensional photonic crystal was analyzed as an all-optical switch since the band gap can be tuned by light, i.e., with a control pulse. The signal beam can thus be dynamically reflected or let through using the control pulse. The band structures were calculated by a Fourier-method, where the material nonlinearity was included in a self-consistent manner.

Waveguides in a two-dimensional photonic crystal with a square-lattice of dielectric rods were examined. The geometry consisted of two parallel defect waveguides formed by missing rows of the dielectric rods. Since there are only a few rows of rods between the two waveguides, they are in general assumed to be coupled, and light coupled into one waveguide will oscillate between the two waveguides with a characteristic period. However, we showed that the waveguides can be completely decoupled for certain geometries (odd number of rods between the waveguides). This can help to reduce the cross-talk between adjacent channels in an integrated optical circuit. Here, the band structures were calculated by the fully vectorial plane wave method (MIT Photonic Bands software). The decoupling was also studied using the finite difference time domain method.

Two-dimensional photonic crystal slabs were studied as a function of the refractive index of the material on top and below the slab. Since the slab is very thin (the thickness is equal to half a period of the photonic crystal), the surrounding material has a strong impact on the band structure of the photonic crystal. The band gap was shown to change with the surrounding material and this effect was proposed to be used for waveguiding. A waveguide constructed by placing stripes of dielectric material on top/below the slab was studied and compared to a conventional defect waveguide. Also, the same effect was studied regarding one-dimensional photonic crystal slabs since also their band gap changes as a function of the refractive index of the material on top/below the slab. Light was shown to be reflected when the surrounding material of a one-dimensional photonic crystal slab was changed abruptly. The band structures of the photonic crystal slabs were calculated using the pseudo spectral method. The performance of the waveguides was studied using the finite difference time domain method. The waveguiding was shown to result from the band gap difference in some cases and from average refractive index difference in some cases.

The geometries of photonic crystal fibers were optimized in order to achieve a large negative dispersion fiber which simultaneously has a large mode area. Usually large negative dispersion fibers have very small mode areas. Thus we studied a dual-core geometry which has a defect ring in the cladding. At a certain wavelength, the shape of the mode changes from being confined to the core to being confined to the defect ring. At this point the effective index of the mode changes abruptly and the dispersion (being proportional to the derivative of the effective index) is very large. Also, the mode areas of this type of fibers are large. The fiber could be used for dispersion compensation or pulse compression in fiber lasers where high intensities are used and thus the mode area of the components has to be large to avoid the nonlinear effects as well as damaging of the fiber. The eigenmodes of the photonic crystal fibers were calculated using the fully vectorial plane wave method.

The effect of the wavelength dependence of gain, nonlinearity and dispersion in high-gain efficiency photonic crystal fiber amplifiers was investigated using the optical nonlinear Schrödinger equation. High-gain efficiency fiber amplifiers usually have small mode-areas in order to maximize the overlap between the mode distribution and the doped core, and thus the dispersion and nonlinearity of these fibers are relatively large and strongly dependent on the wavelength. The wavelength dependence of the parameters was shown to create asymmetry to the spectrum and chirp, but to have a moderating effect on the pulse broadening. Pulse compression or dispersion compensation may be affected by the asymmetrical chirping. The effect of the wavelength dependence of gain and dispersion was shown to be of less importance compared to the effect of the wavelength dependence of nonlinearity.

In the future, photonic crystal components will by widely used in optical tele-

communications. Since the invention of the concept of photonic crystal in the end of the 80's, their properties have been studied intensively. New applications have been proposed and realized. The only components that are so far in commercial use are the photonic crystal fibers. They have many extraordinary properties that cannot be achieved using conventional fibers and thus will have a profound effect on the fiber optics industry. In the near future, other photonic crystal components, such as fiber lasers, will also be brought into market.

Appendix A

Fourier method for nonlinear materials

The dielectric profile $\varepsilon(y)$ (see Fig. 4.1) of the periodic 1D photonic crystal can be represented as a Fourier-series

$$\varepsilon(y) = \sum_{n=-2N}^{2N} \varepsilon_n e^{iK_n y}, \tag{A.1}$$

where $K_n = 2\pi n/P$ and

$$\varepsilon_n = \frac{1}{P}\int_{-P/2}^{P/2} \varepsilon(y) e^{-iK_n y} dy \tag{A.2}$$

are the Fourier-coefficients. The Fourier-coefficients for a 1D photonic crystal where the ε_2-material is nonlinear are

$$\varepsilon_n^{NL} = \frac{1}{P}\left[\int_{-l/2}^{l/2} (\varepsilon_2 + \chi^{(3)} I(y)) e^{-iK_n y} dy + 2\int_{l/2}^{P/2} \varepsilon_1 e^{-iK_n y} dy\right], \tag{A.3}$$

where the first part represents the region where the material is nonlinear. Thus, the Fourier-coefficients can be written as

$$\varepsilon_n^{NL} = \varepsilon_n^{LIN} + \frac{1}{P}\int_{-l/2}^{l/2} \chi^{(3)} I(y) e^{-iK_n y} dy \tag{A.4}$$

The intensity $I(y)$ is represented as a Fourier-series

$$I(y) = \sum_{m=-2N}^{2N} I_m e^{ik_m y}, \tag{A.5}$$

where $k_m = k_0 + 2\pi m/P$. The second term in Eq. (A.4) becomes

$$\begin{aligned}
&\frac{1}{P}\int_{-l/2}^{l/2}\chi^{(3)}\sum_{m=-2N}^{2N} I_m e^{i(k_m-K_n)y}dy \\
=&\frac{1}{P}\int_{-l/2}^{l/2}\chi^{(3)}\sum_{m=-2N}^{2N} I_m e^{i(k_0+2\pi(m-n)/P)y}dy \\
=&\chi^{(3)}\sum_{m=-2N}^{2N} I_m \int_{-l/2}^{l/2} e^{i(k_0+2\pi(m-n)/P)y}dy \\
=&\chi^{(3)}\sum_{m=-2N}^{2N} I_m \frac{2\sin\{[k_0+2\pi(m-n)/P]l/2\}}{P[k_0+2\pi(m-n)/P]}
\end{aligned} \tag{A.6}$$

When a normalized wavevector $x = k_0 P/(2\pi)$ is used the term becomes

$$\begin{aligned}
&\chi^{(3)}\sum_{m=-2N}^{2N} I_m \frac{2\sin\{[2\pi x/P+2\pi(m-n)/P]l/2\}}{P[2\pi x/P+2\pi(m-n)/P]} \\
=&\chi^{(3)}\sum_{m=-2N}^{2N} I_m \frac{2\sin[\pi(x+m-n)l/P]}{\pi(x+m-n)},
\end{aligned} \tag{A.7}$$

which can be substituted into Eq. (A.4).

Appendix B

Derivation of the optical nonlinear Schrödinger equation

The basic steps of the derivation of the propagation equation called the optical nonlinear Schrödinger equation are shown here following the approach of Ref. [94].

B.1 The wave equation

The optical nonlinear Schrödinger equation is deduced from the Maxwell's equations (in SI units) for the electric and magnetic fields $\mathbf{E}(\mathbf{r}, t)$ and $\mathbf{H}(\mathbf{r}, t)$, electric flux density $\mathbf{D}(\mathbf{r}, t)$, and magnetic flux density $\mathbf{B}(\mathbf{r}, t)$ assuming that there are no free charges or currents

$$\nabla \times \mathbf{E}(\mathbf{r}, t) = -\frac{\partial \mathbf{B}(\mathbf{r}, t)}{\partial t} \tag{B.1}$$

$$\nabla \times \mathbf{H}(\mathbf{r}, t) = \frac{\partial \mathbf{D}(\mathbf{r}, t)}{\partial t} \tag{B.2}$$

$$\nabla \cdot \mathbf{D} = 0 \tag{B.3}$$

$$\nabla \cdot \mathbf{B} = 0 \tag{B.4}$$

and the constitutive relations assuming a nonmagnetic medium

$$\mathbf{D} = \varepsilon_0 \mathbf{E} + \mathbf{P} \tag{B.5}$$

$$\mathbf{B} = \mu_0 \mathbf{H}, \tag{B.6}$$

where $\mathbf{P}$ is the induced electric polarization. One takes the curl of Eq. (B.1) and substitutes Eqs. (B.2)–(B.6) into it in order to eliminate the magnetic field, and the magnetic and electric flux densities. This results in the wave equation

$$\nabla \times \nabla \times \mathbf{E} = -\frac{1}{c^2}\frac{\partial^2 \mathbf{E}}{\partial t^2} - \mu_0 \frac{\partial^2 \mathbf{P}}{\partial t^2} \tag{B.7}$$

where $c = 1/\sqrt{\mu_0 \varepsilon_0}$ is the velocity of light in vacuum. Eq. (B.7) can be transformed into

$$\nabla^2 \mathbf{E} - \frac{1}{c^2}\frac{\partial^2 \mathbf{E}}{\partial t^2} = \mu_0 \frac{\partial^2 \mathbf{P}}{\partial t^2} \tag{B.8}$$

since $\nabla \times \nabla \times \mathbf{E} = \nabla(\nabla \cdot \mathbf{E}) - \nabla^2 \mathbf{E} = -\nabla^2 \mathbf{E}$ when a uniform material is assumed. The last step is derived using Eq. (B.3), where the magnetic flux density is written as $\mathbf{D} = \varepsilon \mathbf{E}$ and ε is the dielectric constant of the material. When the material is assumed to be uniform, ε is constant, and thus $\nabla \cdot (\varepsilon \mathbf{E}) = \varepsilon(\nabla \cdot \mathbf{E}) = 0$ indicating that $\nabla \cdot \mathbf{E} = 0$.

B.2 Nonlinearity

The nonlinearity arises because the bound electrons of the material move anharmonically with the applied electric field when light intensity is high. Thus the polarization $\mathbf{P}$ is not linearly dependent on the electric field. For silica fibers the induced polarization can be taken to consist of two parts

$$\mathbf{P}(\mathbf{r}, t) = \mathbf{P}_L(\mathbf{r}, t) + \mathbf{P}_{NL}(\mathbf{r}, t), \tag{B.9}$$

where the linear and nonlinear parts are

$$\mathbf{P}_L(\mathbf{r}, t) = \varepsilon_0 \int_{-\infty}^{\infty} \chi^{(1)}(t - t') \cdot \mathbf{E}(\mathbf{r}, t') dt' \tag{B.10}$$

$$\mathbf{P}_{NL}(\mathbf{r}, t) = \varepsilon_0 \int\int\int_{-\infty}^{\infty} \chi^{(3)}(t - t_1, t - t_2, t - t_3) \cdot \mathbf{E}(\mathbf{r}, t_1)\mathbf{E}(\mathbf{r}, t_2)\mathbf{E}(\mathbf{r}, t_3) dt_1 dt_2 dt_3, \tag{B.11}$$

respectively. The linear part represents the refractive index and attenuation of the material and the nonlinear polarization includes the intensity dependent nonlinear effects. The third order susceptibility can be approximated by [195]

$$\chi^{(3)}(t - t_1, t - t_2, t - t_3) = \chi^{(3)} R(t - t_1)\delta(t - t_2)\delta(t - t_3), \tag{B.12}$$

where

$$R(t) = (1 - f_R)\delta(t) + f_R \frac{\tau_1^2 + \tau_2^2}{\tau_1 \tau_2} e^{-t/\tau_2} \sin(t/\tau_1) \tag{B.13}$$

is the nonlinear response function which includes the Raman response. For silica fibers the parameter values for the Raman response function are $\tau_1 = 12.2$ fs and $\tau_2 = 32$ fs.

B.3 Dispersion

The dispersion terms can be derived by considering the wave equation (B.8) in the Fourier-domain (and forgetting the nonlinear polarization for a while). The electric field is transformed into the Fourier-domain as

$$\tilde{\mathbf{E}}(\mathbf{r}, \omega - \omega_0) = \int_{-\infty}^{\infty} \mathbf{E}(\mathbf{r}, t) e^{i(\omega-\omega_0)t} dt \tag{B.14}$$

and it is substituted into Eq. (B.8) resulting in an equation

$$\nabla^2 \tilde{\mathbf{E}} + \varepsilon(\omega) \frac{\omega^2}{c^2} \tilde{\mathbf{E}} = 0, \tag{B.15}$$

where $\varepsilon(\omega) = 1 + \chi^{(1)}(\omega)$. The electric field is assumed to have a form which allows for the separation of variables

$$\tilde{\mathbf{E}}(\mathbf{r}, \omega - \omega_0) = F(x, y) \tilde{A}(z, \omega - \omega_0) e^{i\beta_0 z}. \tag{B.16}$$

Here, $\tilde{A}(z, \omega - \omega_0)$ is the slowly varying envelope of the pulse and thus the second derivative $\partial^2 \tilde{A}/\partial z^2$ can be neglected. Equation (B.8) can be divided into two equations

$$\frac{\partial^2 F}{\partial x^2} + \frac{\partial^2 F}{\partial y^2} + [\varepsilon(\omega) k_0^2 - \tilde{\beta}^2] F = 0 \tag{B.17}$$

$$2i\beta_0 \frac{\partial \tilde{A}}{\partial z} + (\tilde{\beta}^2 - \beta_0^2) \tilde{A} = 0, \tag{B.18}$$

where $k_0 = \omega/c$ and $\tilde{\beta}$ is the constant needed for the separation of the variables. The transverse mode distribution is solved from Eq. (B.17) giving an eigenvalue $\tilde{\beta}$, which is the propagation constant of the mode. In the first order of perturbation, the mode propagation constant is taken to be

$$\tilde{\beta}(\omega) = \beta(\omega) + \Delta\beta, \tag{B.19}$$

where $\Delta\beta$ depends on the mode distribution. The forward propagation of the eigenmode is solved from Eq. (B.18), where the approximation $\tilde{\beta}^2 - \beta_0^2 \approx 2\beta_0(\tilde{\beta} - \beta_0)$ is made, resulting in

$$\frac{\partial \tilde{A}}{\partial z} = i[\beta(\omega) - \Delta\beta - \beta_0] \tilde{A}. \tag{B.20}$$

The wavenumber is expanded in a Taylor series around the center frequency of the pulse

$$\beta(\omega) = \beta_0 + (\omega - \omega_0)\beta_1 + \frac{1}{2}(\omega - \omega_0)^2 \beta_2 + \frac{1}{6}(\omega - \omega_0)^3 \beta_3 + \ldots, \tag{B.21}$$

where the derivatives

$$\beta_n = \left(\frac{d^n \beta}{d\omega^n}\right)_{\omega=\omega_0} \tag{B.22}$$

are the dispersion parameters of the fiber. Finally, Eq. (B.21) is substituted in Eq. (B.20), and the envelope function is transformed back into the time domain

$$A(z,t) = \frac{1}{2\pi}\int_{-\infty}^{\infty} \tilde{A}(z,\omega-\omega_0)e^{-i(\omega-\omega_0)t}d\omega, \tag{B.23}$$

which leads to

$$\frac{\partial A}{\partial z} = -\beta_1\frac{\partial A}{\partial t} - \frac{i}{2}\beta_2\frac{\partial^2 A}{\partial t^2} + \cdots + i\Delta\beta A. \tag{B.24}$$

The nonlinear effects are included in the term with $\Delta\beta$.

B.4 Optical nonlinear Schrödinger equation

When the nonlinear terms are included in Eq. (B.24), it becomes

$$\begin{aligned}\frac{\partial A}{\partial z} = &-\sum_{n=1}^{M}\frac{i^{n+1}}{n!}\beta_n\frac{\partial^n A}{\partial t^n} - \frac{\alpha A}{2} \\ &+ i\gamma\left(1+\frac{i}{\omega_0}\frac{\partial}{\partial t}\right)A\int_{-\infty}^{\infty} R(t')|A(z,t-t')|^2 dt'.\end{aligned} \tag{B.25}$$

The derivation is shown in Refs. [195, 196]. Equation (B.25) is the optical nonlinear Schrödinger equation.

References

[1] H. Ghiradella, Appl. Opt. **30**, 3492 (1991).

[2] E. Yablonovitch, Phys. Rev. Lett. **58**, 2059 (1987).

[3] S. John, Phys. Rev. Lett. **58**, 2486 (1987).

[4] E. Yablonovitch and T. J. Gitter, Phys. Rev. Lett. **63**, 1950 (1989).

[5] K. M. Ho, C. T. Chan, and C. M. Soukoulis, Phys. Rev. Lett. **65**, 3152 (1990).

[6] E. Yablonovitch, T. J. Gmitter, and K. M. Leung, Phys. Rev. Lett. **67**, 2295 (1991).

[7] E. Yablonovitch, T. J. Gmitter, R. D. Meade, A. M. Rappe, K. D. Brommer, and J. D. Joannopoulos, Phys. Rev. Lett. **67**, 3380 (1991).

[8] E. Yablonovitch, J. Opt. Soc. Am. B **10**, 283 (1993).

[9] S. L. McCall, P. M. Platzman, R. Dalichaouch, D. Smith, and S. Schultz, Phys. Rev. Lett. **67**, 2017 (1991).

[10] W. M. Robertson, G. Arjavalingam, R. D. Meade, K. D. Brommer, A. M. Rappe, and J. D. Joannopoulos, Phys. Rev. Lett. **68**, 2023 (1992).

[11] M. Plihal and A. A. Maradudin, Phys. Rev. B **44**, 8565 (1991).

[12] P. R. Villeneuve and M. Piché, Phys. Rev. B **46**, 4969 (1992).

[13] J. D. Joannopoulos, R. D. Meade, and J. N. Winn, *Photonic Crystals - Molding the Flow of Light* (Princeton University Press, Princeton, 1995).

[14] A. Mekis, J. C. Chen, I. Kurland, S. Fan, P. R. Villeneuve, and J. D. Joannopoulos, Phys. Rev. Lett. **77**, 3787 (1996).

[15] K. A. McIntosh, L. J. Mahoney, K. M. Molvar, O. B. McMahon, S. Verghese, M. Rothschild, and E. R. Brown, Appl. Phys. Lett. **70**, 2937 (1997).

[16] S. Y. Lin, J. G. Fleming, D. L. Hetherington, B. K. Smith, R. Biswas, K. M. Ho, M. M. Sigalas, W. Zubrzycki, S. R. Kurtz, and J. Bur, Nature **394**, 251 (1998).

[17] J. G. Fleming and S.-Y. Lin, Opt. Lett. **24**, 49 (1999).

[18] S. Noda, N. Yamamoto, H. Kobayashi, M. Okano, and K. Tomoda, Appl. Phys. Lett. **75**, 905 (1999).

[19] J. D. Joannopoulos, P. R. Villeneuve, and S. Fan, Nature **386**, 143 (1997).

[20] G. Parker and M. Charlton, Physics World **August**, 29 (2000).

[21] S. Noda, MRS Bulletin **August**, 681 (2001).

[22] S. Noda, M. Imada, M. Okano, S. Ogawa, M. Mochizuki, and A. Chutinan, IEEE J. Quantum Electron. **38**, 726 (2002).

[23] S.-Y. Lin, E. Chow, V. Hietala, P. R. Villeneuve, and J. D. Joannopoulos, Science **282**, 274 (1998).

[24] T. Baba, N. Fukaya, and J. Yonekura, Electron. Lett. **35**, 654 (1999).

[25] J. S. Foresi, P. R. Villeneuve, J. Ferrara, E. R. Thoen, G. Steinmeyer, S. Fan, J. D. Joannopoulos, L. C. Kimerling, H. I. Smith, and E. P. Ippen, Nature **390**, 143 (1997).

[26] Y. Akahane, T. Asano, B.-S. Song, and S. Noda, Nature **425**, 944 (2003).

[27] B.-S. Song, S. Noda, T. Asano, and Y. Akahane, Nature Materials **4**, 207 (2005).

[28] S. Noda, K. Tomoda, N. Yamamoto, and A. Chutinan, Science **289**, 604 (2000).

[29] O. Painter, R. K. Lee, A. Scherer, A. Yariv, J. D. O'Brien, P. D. Dapkus, and I. Kim, Science **284**, 1819 (1999).

[30] M. Imada, S. Noda, A. Chutinan, and T. Tokuda, Appl. Phys. Lett. **75**, 316 (1999).

[31] R. Colombelli, K. Srinivasan, M. Troccoli, O. Painter, C. F. Gmachl, D. M. Tennant, A. M. Sergent, D. L. Sivco, A. Y. Cho, and F. Capasso, Science **302**, 1374 (2003).

[32] S. Ogawa, M. Imada, S. Yoshimoto, M. Okano, and S. Noda, Science **305**, 227 (2004).

[33] M. Soljačić and J. D. Joannopoulos, Nature Materials **3**, 211 (2004).

[34] J. C. Knight, J. Broeng, T. A. Birks, and P. St. J. Russell, Science **282**, 1476 (1998).

[35] R. F. Cregan, B. J. Mangan, J. C. Knight, T. A. Birks, P. St. J. Russell, P. J. Roberts, and D. C. Allan, Science **285**, 1537 (1999).

[36] J. C. Knight, T. A. Birks, P. St. J. Russell, and D. M. Atkin, Opt. Lett. **21**, 1547 (1996).

[37] T. A. Birks, J. C. Knight, and P. St. J. Russell, Opt. Lett. **22**, 961 (1997).

[38] N. A. Mortensen, J. R. Folkenberg, M. D. Nielsen, and K. P. Hansen, Opt. Lett. **28**, 1879 (2003).

[39] D. Mogilevtsev, T. A. Birks, and P. St. J. Russell, Opt. Lett. **23**, 1662 (1998).

[40] J. K. Ranka, R. S. Windeler, and A. J. Stentz, Opt. Lett. **25**, 25 (2000).

[41] A. Ferrando, E. Silvestre, J. J. Miret, and P. Andrés, Opt. Lett. **25**, 790 (2000).

[42] J. C. Knight, J. Arriaga, T. A. Birks, A. Ortigosa-Blanch, W. J. Wadsworth, and P. St. J. Russell, IEEE Photon. Tech. Lett. **12**, 807 (2000).

[43] J. C. Knight, T. A. Birks, R. F. Cregan, P. St. J. Russell, and J.-P. de Sandro, Electron. Lett. **34**, 1347 (1998).

[44] N. G. R. Broderick, T. M. Monro, P. J. Bennett, and D. J. Richardson, Opt. Lett. **24**, 1395 (1999).

[45] P. Russell, Science **299**, 358 (2003).

[46] J. C. Knight, Nature **424**, 847 (2003).

[47] J. Limpert, A. Liem, T. Schreiber, F. Röser, H. Zellmer, A. Tünnermann, and F. Schiller, Photonics Spectra **May**, 54 (2004).

[48] A. Blanco *et al.*, Nature **405**, 437 (2000).

[49] E. Chow, S. Y. Lin, S. G. Johnson, P. R. Villeneuve, J. D. Joannopoulos, J. R. Wendt, G. A. Vawter, W. Zubrzycki, H. Hou, and A. Alleman, Nature **407**, 983 (2000).

[50] I. R. Matías, I. Del Villar, F. J. Arregui, and R. O. Claus, Opt. Lett. **28**, 1099 (2003).

[51] C. J. M. Smith, H. Benisty, S. Olivier, M. Rattier, C. Weisbuch, T. F. Krauss, R. M. De La Rue, R. Houdré, and U. Oesterle, Appl. Phys. Lett. **77**, 2813 (2000).

[52] B. E. A. Saleh and M. C. Teich, *Fundamentals of photonics* (Wiley, New York, 1991).

[53] S.-Y. Lin, V. M. Hietala, S. K. Lyo, and A. Zaslavsky, Appl. Phys. Lett. **68**, 3233 (1996).

[54] P. Lodahl, A. F. van Driel, I. S. Nikolaev, A. Irman, K. Overgaag, D. Vanmaekelbergh, and W. L. Vos, Nature **430**, 654 (2004).

[55] C. Hermann and O. Hess, J. Opt. Soc. Am. B **19**, 3013 (2002).

[56] S. Noda, A. Chutinan, and M. Imada, Nature **407**, 608 (2000).

[57] B.-S. Song, S. Noda, and T. Asano, Science **300**, 1537 (2003).

[58] K. Busch and S. John, Phys. Rev. Lett. **83**, 967 (1999).

[59] M. J. Escuti, J. Qi, and G. P. Crawford, Opt. Lett. **28**, 522 (2003).

[60] M. Scalora, J. P. Dowling, C. M. Bowden, and M. J. Bloemer, Phys. Rev. Lett. **73**, 1368 (1994).

[61] S. Radic, N. George, and G. P. Agrawal, Opt. Lett. **19**, 1789 (1994).

[62] M. D. Tocci, M. J. Bloemer, M. Scalora, J. P. Dowling, and C. M. Bowden, Appl. Phys. Lett. **66**, 2324 (1995).

[63] P. Tran, Opt. Lett. **21**, 1138 (1996).

[64] S. Scholz, O. Hess, and R. Rühle, Optics Express **3**, 28 (1998).

[65] P. Tran, J. Opt. Soc. Am. B **16**, 70 (1999).

[66] M. Cada, J. He, B. Acklin, M. Proctor, D. Martin, F. Morier-Genoud, M.-A. Dupertuis, and J. M. Glinski, Appl. Phys. Lett. **60**, 404 (1992).

[67] N. D. Sankey, D. F. Prelewitz, and T. G. Brown, Appl. Phys. Lett. **60**, 1427 (1992).

[68] A. Haché and M. Bourgeois, Appl. Phys. Lett. **77**, 4089 (2000).

[69] M. Shimizu and T. Ishihara, Appl. Phys. Lett. **80**, 2836 (2002).

[70] S. W. Leonard, H. M. van Driel, J. Schilling, and R. B. Wehrspoon, Phys. Rev. B **66**, 161102(R) (2002).

[71] F. Raineri, C. Cojocaru, P. Monnier, A. Levenson, R. Raj, C. Seassal, X. Letartre, and P. Viktorovitch, Appl. Phys. Lett. **85**, 1880 (2004).

[72] A. D. Bristow, J.-P. R. Wells, W. H. Fan, A. M. Fox, M. S. Skolnick, D. M. Whittaker, A. Tahraoui, T. F. Krauss, and J. S. Roberts, Appl. Phys. Lett. **83**, 851 (2003).

[73] X. Hu, Y. Liu, J. Tian, B. Cheng, and D. Zhang, Appl. Phys. Lett. **86**, 121102 (2005).

[74] H. Nakamura *et al.*, Optics Express **12**, 6606 (2004).

[75] D. A. Mazurenko, R. Kerst, J. I. Dijkhuis, A. V. Akimov, V. G. Golubev, D. A. Kurdyukov, A. B. Pevtsov, and A. V. Sel'kin, Phys. Rev. Lett. **91**, 213903 (2003).

[76] J. He, M. Cada, M.-A. Dupertuis, D. Martin, F. Morier-Genoud, C. Rolland, and A. J. SpringThorpe, Appl. Phys. Lett. **63**, 866 (1993).

[77] B. Acklin, M. Cada, J. He, and M.-A. Dupertuis, Appl. Phys. Lett. **63**, 2177 (1993).

[78] E. Centeno and D. Felbacq, Phys. Rev. B **62**, R7683 (2000).

[79] M. Soljačić, M. Ibanescu, S. G. Johnson, Y. Fink, and J. D. Joannopoulos, Phys. Rev. E **66**, 055601(R) (2002).

[80] M. F. Yanik, S. Fan, and M. Soljačić, Appl. Phys. Lett. **83**, 2739 (2003).

[81] M. Notomi, A. Shinya, S. Mitsugi, G. Kira, E. Kuramochi, and T. Tanabe, Optics Express **13**, 2678 (2005).

[82] S.-Y. Lin and J. G. Fleming, J. Lightwave Technol. **17**, 1944 (1999).

[83] S. Noda, N. Yamamoto, M. Imada, H. Kobayashi, and M. Okano, J. Lightwave Technol. **17**, 1948 (1999).

[84] K. Aoki, H. T. Miyazaki, H. Hirayama, K. Inoshita, T. Baba, K. Sakoda, N. Shinya, and Y. Aoyagi, Nature Materials **2**, 117 (2003).

[85] Y. A. Vlasov, X.-Z. Bo, J. C. Sturm, and D. J. Norris, Nature **414**, 289 (2001).

[86] M. Campbell, D. N. Sharp, M. T. Harrison, R. G. Denning, and A. J. Turberfield, Nature **404**, 53 (2000).

[87] M. Maldovan and E. L. Thomas, Nature Materials **3**, 593 (2004).

[88] O. Toader and S. John, Science **292**, 1133 (2001).

[89] S. G. Johnson and J. D. Joannopoulos, Appl. Phys. Lett. **77**, 3490 (2000).

[90] M. Qi, E. Lidorikis, P. T. Rakich, S. G. Johnson, J. D. Joannopoulos, E. P. Ippen, and H. I. Smith, Nature **429**, 538 (2004).

[91] D. Roundy and J. Joannopoulos, Appl. Phys. Lett. **82**, 3835 (2003).

[92] U. Grüning, V. Lehmann, S. Ottow, and K. Busch, Appl. Phys. Lett. **68**, 747 (1996).

[93] H.-B. Lin, R. J. Tonucci, and A. J. Campillo, Appl. Phys. Lett. **68**, 2927 (1996).

[94] G. P. Agrawal, *Nonlinear fiber optics* (Academic, San Diego, 1995).

[95] G. P. Agrawal, *Fiber-optic communication systems* (Wiley, New York, 1997).

[96] M. D. Nielsen and N. A. Mortensen, Opt. Express **11**, 2762 (2003).

[97] N. A. Mortensen and J. R. Folkenberg, J. Opt. A: Pure Appl. Opt. **5**, 163 (2003).

[98] N. A. Mortensen, M. D. Nielsen, J. R. Folkenberg, A. Petersson, and H. R. Simonsen, Opt. Lett. **28**, 393 (2003).

[99] D. G. Ouzounov, K. D. Moll, M. A. Foster, W. R. Zipfel, W. W. Webb, and A. L. Gaeta, Opt. Lett. **27**, 1513 (2002).

[100] M. D. Nielsen, J. R. Folkenberg, and N. A. Mortensen, Electron. Lett. **39**, 1802 (2003).

[101] S. Coen, A. H. L. Chau, R. Leonhardt, J. D. Harvey, J. C. Knight, W. J. Wadsworth, and P. St. J. Russell, Opt. Lett. **26**, 1356 (2001).

[102] P. A. Champert, S. V. Popov, and J. R. Taylor, Opt. Lett. **27**, 122 (2002).

[103] J. H. V. Price, W. Belardi, T. M. Monro, A. Malinowski, A. Piper, and D. J. Richardson, Opt. Lett. **10**, 382 (2002).

[104] W. J. Wadsworth, J. C. Knight, A. Origosa-Blanch, J. Arriaga, E. Silvestre, and P. St. J. Russell, Electron. Lett. **36**, 53 (2000).

[105] A. V. Husakou and J. Herrmann, Phys. Rev. Lett. **87**, 203901 (2001).

[106] A. L. Gaeta, Opt. Lett. **27**, 924 (2002).

[107] J. Herrmann, U. Griebner, N. Zhavoronkov, A. Husakou, D. Nickel, J. C. Knight, W. J. Wadsworth, P. St. J. Russell, and G. Korn, Phys. Rev. Lett. **88**, 173901 (2002).

[108] X. Gu, L. Xu, M. Kimmel, E. Zeek, P. O'Shea, A. P. Shreenath, R. Trebino, and R. S. Windeler, Opt. Lett. **27**, 174 (2002).

[109] J. M. Dudley and S. Coen, Opt. Lett. **27**, 180 (2002).

[110] G. Genty, M. Lehtonen, H. Ludvigsen, J. Broeng, and M. Kaivola, Opt. Express **10**, 1083 (2002).

[111] K. L. Corwin, N. R. Newbury, J. M. Dudley, S. Coen, S. A. Diddams, K. Weber, and R. S. Windeler, Phys. Rev. Lett. **90**, 113904 (2003).

[112] G. Chang, T. B. Norris, and H. G. Winful, Opt. Lett. **28**, 546 (2003).

[113] M. Lehtonen, G. Genty, H. Ludvigsen, and M. Kaivola, Appl. Phys. Lett. **82**, 2197 (2003).

[114] N. R. Newbury, B. R. Washburn, K. L. Corwin, and R. S. Windeler, Opt. Lett. **28**, 944 (2003).

[115] A. V. Avdokhin, S. V. Popov, and J. R. Taylor, Opt. Lett. **28**, 1353 (2003).

[116] M. A. Foster and A. L. Gaeta, Opt. Express **12**, 3137 (2004).

[117] G. Genty, M. Lehtonen, H. Ludvigsen, and M. Kaivola, Opt. Express **12**, 3471 (2004).

[118] A. Ferrando, E. Silvestre, P. Andrés, J. J. Miret, and M. V. Andrés, Opt. Express **9**, 687 (2001).

[119] G. Renversez, B. Kuhlmey, and R. McPhedran, Opt. Lett. **28**, 989 (2003).

[120] W. H. Reeves, J. C. Knight, P. St. J. Russell, and P. J. Roberts, Opt. Express **10**, 609 (2002).

[121] W. H. Reeves, D. V. Skryabin, F. Biancalana, J. C. Knight, P. St. J. Russell, F. G. Omanetto, A. Efimov, and A. J. Taylor, Nature **424**, 511 (2003).

[122] T. A. Birks, D. Mogilevtsev, J. C. Knight, and P. St. J. Russell, IEEE Photon. Tech. Lett. **11**, 674 (1999).

[123] L. P. Shen, W.-P. Huang, G. X. Chen, and S. S. Jian, IEEE Photon. Tech. Lett. **15**, 540 (2003).

[124] L. P. Shen, W.-P. Huang, and S. S. Jian, J. Lightwave Tech. **21**, 1644 (2003).

[125] R. K. Sinha and S. K. Varshney, Microwave and Optical Tech. Lett. **37**, 129 (2003).

[126] F. Poli, A. Cucinotta, M. Fuochi, S. Selleri, and L. Vincetti, J. Opt. Soc. Am. A **20**, 1958 (2003)).

[127] J. Broeng, S. E. Barkou, T. Søndergaard, and A. Bjarklev, Opt. Lett. **25**, 96 (2000).

[128] C. M. Smith, N. Venkataraman, M. T. Gallagher, D. Müller, J. A. West, N. F. Borrelli, D. C. Allan, and K. W. Koch, Nature **424**, 657 (2003).

[129] G. Humbert, J. C. Knight, G. Bouwmans, P. St. J. Russell, D. P. Williams, P. J. Roberts, and B. J. Mangan, Opt. Express **12**, 1477 (2004).

[130] Y. Xu and A. Yariv, Opt. Lett. **28**, 1885 (2003).

[131] F. Benabid, J. C. Knight, G. Antonopoulos, and P. St. J. Russell, Science **298**, 399 (2002).

[132] F. Benabid, F. Couny, J. C. Knight, T. A. Birks, and P. St. J. Russell, Nature **434**, 488 (2005).

[133] T. Ritari, J. Tuominen, H. Ludvigsen, J. C. Petersen, T. Sørensen, T. P. Hansen, and H. R. Simonsen, Opt. Express **12**, 4080 (2004).

[134] F. Benabid, J. C. Knight, and P. St. J. Russell, Opt. Express **10**, 1195 (2002).

[135] W. N. MacPherson *et al.*, Opt. Commun. **193**, 97 (2001).

[136] T. M. Monro, W. Belardi, K. Furusawa, J. C. Baggett, N. G. R. Broderick, and D. J. Richardson, Meas. Sci. Technol. **12**, 854 (2001).

[137] I. Hartl, X. D. Li, C. Chudoba, R. K. Ghanta, T. H. Ko, J. G. Fujimoto, J. K. Ranka, and R. S. Windeler, Opt. Lett. **26**, 608 (2001).

[138] R. Holzwarth, M. Zimmermann, Th. Udem, T. W. Hänsch, P. Russbüldt, K. Gäbel, R. Poprawe, J. C. Knight, W. J. Wadsworth, and P. St. J. Russell, Opt. Lett. **26**, 1376 (2001).

[139] Th. Udem, R. Holzwarth, and T. W. Hänsch, Nature **416**, 233 (2002).

[140] P. Petropoulos, T. M. Monro, W. Belardi, K. Furusawa, J. H. Lee, and D. J. Richardson, Opt. Lett. **26**, 1233 (2001).

[141] B. J. Mangan, J. Arriaga, T. A. Birks, J. C. Knight, and P. St. J. Russell, Opt. Lett. **26**, 1469 (2001).

[142] B. J. Eggleton, C. Kerbage, P. S. Westbrook, R. S. Windeler, and A. Hale, Opt. Express **9**, 698 (2001).

[143] K. G. Hougaard, J. Broeng, and A. Bjarklev, Electron. Lett. **39**, 599 (2003).

[144] K. Furusawa, T. Kogure, T. M. Monro, and D. J. Richardson, Opt. Express **12**, 3452 (2004).

[145] J. Limpert, A. Liem, M. Reich, T. Schreiber, S. Nolte, H. Zellmer, A. Tünnermann, J. Broeng, A. Petersson, and C. Jakobsen, Opt. Express **12**, 1313 (2004).

[146] A. Shirakawa, J. Ota, M. Musha, K. Nakagawa, K. Ueda, J. R. Folkenberg, and J. Broeng, Opt. Express **13**, 1221 (2005).

[147] W. J. Wadsworth, J. C. Knight, W. H. Reeves, P. St. J. Russell, and J. Arriaga, Electron. Lett. **36**, 1452 (2000).

[148] J. K. S. C. C. Renaud, K. Furusawa, J. A. A.-C. R. Selvas, D. J. Richardson, and J. Nilsson, Electronics Lett. **37**, 1116 (2001).

[149] K. Furusawa, T. M. Monro, P. Petropoulos, and D. J. Richarson, Electron. Lett. **37**, 560 (2001).

[150] K. Furusawa, T. Kogure, J. K. Sahu, J. H. Lee, T. M. Monro, and D. J. Richardson, IEEE Photon. Tech. Lett. **17**, 25 (2005).

[151] K. Furusawa, A. Malinowski, T. M. M. J. H. V. Price, J. K. Sahu, J. Nilsson, and D. J. Richardson, Opt. Express **9**, 714 (2001)).

[152] P. Glas and D. Fischer, Opt. Express **10**, 286 (2002).

[153] W. J. Wadsworth, R. M. Percival, J. C. K. G. Bouwmans, and P. St. J. Russell, Opt. Express **11**, 48 (2003).

[154] J. Canning, N. Groothoff, E. Buckley, T. Ryan, K. Lyytikainen, and J. Digweed, Opt. Express **11**, 1995 (2003).

[155] J. Limpert *et al.*, Opt. Express **13**, 1055 (2005).

[156] A. Argyros, M. A. van Eijkelenborg, S. D. Jackson, and R. P. Mildren, Opt. Lett. **29**, 1882 (2004)).

[157] J. H. V. Price, K. Furusawa, T. M. Monro, L. Lefort, and D. J. Richardson, J. Opt. Soc. Am. B **19**, 1286 (2002).

[158] P. J. Bennett, T. M. Monro, and D. J. Richardson, Opt. Lett. **24**, 1203 (1999).

[159] P. Kaiser and H. W. Astle, Bell Syst. Tech. J. **53**, 1021 (1974).

[160] M. A. van Eijkelenborg *et al.*, Opt. Express **9**, 319 (2001).

[161] K. M. Kiang, K. Frampton, T. M. Monro, R. Moore, J. Tucknott, D. W. Hewak, D. J. Richardson, and H. N. Rutt, Electron. Lett. **38**, 546 (2002).

[162] V. V. R. K. Kumar, A. K. George, W. H. Reeves, J. C. Knight, P. St. J. Russell, F. G. Omenetto, and A. J. Taylor, Opt. Express **10**, 1520 (2002).

[163] A. R. Baghai-Wadji, *Lecture notes* (Vienna University of Technology, Vienna, 1994).

[164] K. Varis and A. R. Baghai-Wadji, ACES J. **19**, 101 (2004).

[165] S. G. Johnson and J. D. Joannopoulos, Opt. Express **8**, 173 (2001).

[166] A. Taflove and S. C. Hagness, *Computational Electrodynamics: The Finite-Difference Time-Domain Method* (Artech House, Boston, 2000).

[167] O. Hess, C. Hermann, and A. Klaedtke, Phys. Stat. Sol. **197**, 605 (2003).

[168] D. A. B. Miller, D. S. Chemla, D. J. Eilenberg, P. W. Smith, A. C. Gossard, and W. Wiegmann, Apl. Phys. Lett. **42**, 925 (1983).

[169] M. Koshiba, J. Lightwave Technol. **19**, 1970 (2001).

[170] M. Tokushima and H. Yamada, Electron. Lett. **37**, 1454 (2001).

[171] S. Boscolo, M. Midrio, and C. G. Someda, IEEE J. Quantum Electron. **38**, 47 (2002).

[172] A. Martinez, F. Cuesta, and J. Marti, IEEE Photonics Technol. Lett. **15**, 694 (2003).

[173] M. Qiu, M. Mulot, M. Swillo, S. Anand, B. Jaskorzynska, A. Karlsson, M. Kamp, and A. Forchel, Appl. Phys. Lett. **83**, 5121 (2003).

[174] S. Kuchinsky, V. Y. Golyatin, A. Y. Kutikov, T. P. Pearsall, and D. Nedeljkovic, IEEE J. Quantum Electron. **38**, 1349 (2002).

[175] F. S.-S. Chien, Y.-J. Hsu, W.-F. Hsieh, and S.-C. Cheng, Opt. Express **12**, 1119 (2004).

[176] S. G. Johnson, S. Fan, P. R. Villeneuve, J. D. Joannopoulos, and L. A. Kolodziejski, Phys. Rev. B **60**, 5751 (1999).

[177] M. Lončar, T. Doll, J. Vučković, and A. Scherer, J. Lightwave Technol. **18**, 1402 (2000).

[178] S. Y. Lin, E. Chow, S. G. Johnson, and J. D. Joannopoulos, Opt. Lett. **25**, 1297 (2000).

[179] S. G. Johnson, P. R. Villeneuve, S. Fan, and J. D. Joannopoulos, Phys. Rev. B **62**, 8212 (2000).

[180] M. Lončar, D. Nedeljković, T. Doll, J. Vučković, A. Scherer, and T. P. Pearsall, Appl. Phys. Lett. **77**, 1937 (2000).

[181] Y. Ni, L. An, J. Peng, and C. Fan, IEEE Photon. Tech. Lett. **16**, 1516 (2004).

[182] F. Gérôme, J.-L. Auguste, and J.-M. Blondy, Opt. Lett. **29**, 2725 (2004).

[183] K. Thyagarajan, R. K. Varshney, P. Palai, A. K. Ghatak, and I. C. Goyal, IEEE Photon. Technol. Lett. **8**, 1510 (1996).

[184] J.-L. Auguste, R. Jindal, J.-M. Blondy, M. Clapeau, J. Marcou, B. Dussardier, G. Monnom, D. B. Ostrowsky, B. P. Pal, and K. Thyagarajan, Electronics Lett. **36**, 1689 (2000).

[185] J. L. Auguste, J. M. Blondy, J. Maury, J. Marcou, B. Dussardier, G. Monnom, R. Jindal, K. Thyagarajan, and B. P. Pal, Opt. Fiber Technol. **8**, 89 (2002).

[186] K. Pande and B. P. Pal, Appl. Opt. **42**, 3785 (2003).

[187] G. Ouyang, Y. Xu, and A. Yariv, Opt. Express **10**, 899 (2002).

[188] T. D. Engeness, M. Ibanescu, S. G. Johnson, O. Weisberg, M. Skorobogatiy, S. Jacobs, and Y. Fink, Opt. Express **11**, 1175 (2003).

[189] C. D. Poole, J. M. Wiesenfeld, D. J. DiGiovanni, and A. M. Vengsarkar, J. Lightwave Technol. **12**, 1746 (1994).

[190] A. H. Gnauck, L. D. Garrett, Y. Danziger, U. Levy, and M. Tur, Electronics Lett. **36**, 1946 (2000).

[191] S. Ramachandran *et al.*, IEEE Photon. Tech. Lett. **13**, 632 (2001).

[192] S. Ghalmi, S. Ramachandran, E. Monberg, Z. Wang, M. Yan, F. Dimarello, W. Reed, P. Wisk, and J. Fleming, Electronics Lett. **38**, 1507 (2002).

[193] A. Cucinotta, F. Poli, and S. Selleri, IEEE Photon. Tech. Lett. **16**, 2027 (2004).

[194] R. Hainberger and S. Watanabe, IEEE Photon. Tech. Lett. **17**, 70 (2005).

[195] K. J. Blow and D. Wood, IEEE J. Quantum Electron. **25**, 2665 (1989).

[196] P. V. Mamyshev and S. V. Chernikov, Opt. Lett. **15**, 1076 (1990).